Supporting Information

Unraveling the Dual Defect Sites in Graphite Carbon Nitride for

Ultra-high Photocatalytic H₂O₂ Evolution

Xu Zhang[a], Peijie Ma[a], Cong Wang*[a], Liyong Gan[b], Xianjie Chen[c], Peng Zhang[d], Yang Wang[b], Hui Li[a], Lihua Wang[a], Xiaoyuan Zhou*[b] and Kun Zheng*[a]

X. Zhang, P.J. Ma, Dr. C. Wang, H. Li, Prof. L. H. Wang, Prof. K. Zheng
Beijing Key Lab of Microstructure and Properties of Solids, Faculty of Materials and Manufacturing, Beijing University of Technology, Beijing, 100124, China
E-mail: smartswang@bjut.edu.cn; kunzheng@bjut.edu.cn

Prof. L.Y. Gan, Prof. X.Y. Zhou, Y. Wang

College of Physics and Institute of Advanced Interdisciplinary Studies
Chongqing University
Chongqing 400044, P. R. China
E-mail: xiaoyuan2013@cqu.edu.cn

Dr. X.J. Chen
State Key Laboratory of Environmental-Friendly Energy Materials, School of Materials Science and Engineering, Southwest University of Science and Technology, Mianyang 621010, China

Prof. Peng Zhang
Key Laboratory of Organic Compound Pollution Control Engineering (MOE), School of Environmental and chemical engineering, Shanghai University, Shanghai 200444, China

1. Experimental section

1.1. Synthesis of samples

All chemicals used in this work are of analytical grade and no further purification is required before use.

Synthesis of pristine g-C$_3$N$_4$ (PCN) and TCN: Briefly, 10 g of urea was put into an alumina crucible with a lid, and the temperature was increased to 550 °C for 2 h in air at a rate of 5 °C min^{-1}. The capacity of the crucibles used in this work were 100 ml. After the crucible was cooled to room temperature, the product was collected and ground into powder, washed with deionized water several times, and vacuum dried at 80 °C for 12 h. The TCN was synthesized by the same method except that the precursor used was thiourea.

Synthesis of cyano-modified g-C$_3$N$_4$ (C≡N-CN): The cyano-modified g-C$_3$N$_4$ was synthesized by heating the supramolecular precursor of urea and thiourea in different ratios. In detail, different mass ratios of urea and thiourea (1:1, 1:2, 1:3, total mass: 10 g) were respectively dispersed in 20 ml of deionized water. After them was fully dissolved, the two solutions were mixed and stirred and dried at 60 °C. Collected the white supramolecular precursor and grinded it into a powder, then place it in a 100 ml crucible with a lid and heat it to 550 °C for 2 h in air with ramping rate of 5 °C min^{-1} (Wrap the crucible with tin foil to maintain tightness). After cooling to room temperature, the obtained powders were washed with ethanol and deionized water

several times and vacuum dry at 80 °C for 12 h. The obtained g-C_3N_4 modified with -C≡N groups were named C≡N-CN, C≡N-CN$_1$ and C≡N-CN$_2$, respectively.

Synthesis of Nv-C≡N-CN: The Nv-C≡N-CN was synthesized by calcining C≡N-CN in a tube furnace under argon atmosphere. 250 mg C≡N-CN was fully milled and heated to 550 °C for 2 h at a heating rate of 5 °C min^{-1} in an argon atmosphere (argon flow rate is 100 ml min^{-1}). After cooling to room temperature, the obtained powders were washed with deionized water and ethanol several times, and vacuum dried at 80 °C for 12 h.

Synthesis of Nv-CN: 250 mg of PCN was heated to 550 °C for 2 h in an argon atmosphere (argon flow rate is 100 ml min^{-1}) at a heating rate of 5 °C min^{-1}. After cooling to room temperature, the obtained powder was washed several times and vacuum dried at 80 °C for 12 h.

1.2. Characterization

The X-ray diffraction (XRD) patterns of the samples were collected on a PANalytical B.V. X'Pert Powder X-ray diffractometer with Cu Kα radiation at 40 kV and 40 mA. The Fourier transform infrared (FTIR) spectra were obtained on Bruker V70 spectrometer. X-ray photoelectron spectroscopy (XPS) measurements were acquired on an ESCALAB 250Xi instrument (Thermo Fisher Scientific) using Al Kα radiation, and the calibration peak was C 1s at 284.8 eV. UV-Vis diffuse reflectance spectroscopy

(DRS) of the samples were collected on Shimadzu UV-3600 instrument with $BaSO_4$ as reference. Solid-state ^{13}C MAS NMR spectra were measured on Bruker AVANCE III 400MHz WB solid-state NMR spectrometer at room temperature. Photoluminescence (PL) spectra were measured on Hitachi F-7000 fluorescence spectrometer with an excitation wavelength of 325 nm. Time-resolved photoluminescence (TRPL) spectra were collected on Edinburgh FLS1000 fluorescence spectrometer with an excitation wavelength of 375 nm. The room temperature electron paramagnetic resonance (EPR) spectra of the samples were measured by JOEL JES-FA200 spectrometer. The C and N content of the samples were measured by an element analyzer (Vario MACRO). The microstructure and surface morphology of the samples were studied by transmission electron microscopy (TEM, TEI-Tecnai-Talos) and scanning electron microscopy (SEM, Thermo Fisher Scientific Quattro S). The N_2 adsorption-desorption isotherms and pore-size distributions of the samples were measured at 77 K using micrometrics Max-II system. Before the experiments, the samples were degassed in a vacuum environment at 180 °C for 10 h, and the specific surface areas of all samples were calculated according to the Brunauer-Emmett-Teller (BET) method. Raman spectra were acquired on a high-resolution confocal Raman spectrometer (RENISHAW inVia) with an excitation laser of 785nm. The spectra were collected by using a ×50 L objective lens for 10 s with a laser spot diameter of about 1 um and power of 0.5mW for all acquisitions.

1.3. Photoelectrochemical measurements

The electrochemical impedance spectroscopy (EIS), photocurrent response, and Mott–Schottky plots were measured on the electrochemical workstation (CHI600A). The electrochemical workstation was a standard three-electrode system, in which the catalyst-coated ITO was the working electrode, the Pt wire was the counter electrode and the saturated calomel electrode was the reference electrode.

1.4. Photocatalytic reduction of O_2 to H_2O_2

20 mg of photocatalyst was placed in 20 ml of pure water ($1g\ L^{-1}$), and ultrasonicated for 30 minutes until the catalyst powder was completely dispersed. After that, O_2 was continuously injected into the solution for 30 min under dark conditions to make the O_2 saturated. After 30 min, the flow rate of O_2 was controlled to 300 ml min^{-1}. The reaction solution was irradiated under a 300 W Xe lamp with 420 nm cutoff film ($\lambda \geq 420$ nm) to start the photoreaction test. The average light intensity was 40 mW cm^{-2}. The entire photoreaction process used a stirrer and circulating water to control the reaction temperature at 25 °C. Every 15min, 1.5 ml of the reaction solution was taken out to remove the photocatalyst by centrifugation and filtration. To explore the influence of H^+ concentration on the reaction, the pH of the reaction solution was adjusted by $HClO_4$ and KOH. Replaced pure water with 10% isopropanol solution for the reaction under sacrificial agent conditions.

In order to explore the influence of different sacrificial agents on the H_2O_2 generation activity under the same conditions, the concentration of BQ and $AgNO_3$ added to the reaction system were both 1mM, and the concentration of TBA added to the reaction

system was 1%. In order to explore the influence of different gases (N_2 or O_2) on the photocatalytic H_2O_2 generation activity, N_2 was continuously injected into the reaction solution under dark conditions for 60 minutes to ensure that there was no residual O_2. After that, the photocatalysis test was carried out under the condition of continuous N_2 flow. Under the same conditions, the 420 nm cutoff film (visible light, $\lambda \geq 420$ nm) of the 300 W Xe lamp was replaced with an AM 1.5G filter (simulate sunlight) to compare the effects of different light sources on the photocatalytic H_2O_2 generation activity. In addition, the decomposition rate of H_2O_2 on different samples were tested in 1 mM H_2O_2 solution.

The amount of H_2O_2 was determined by iodometry.[1] 0.5 ml of 0.4 mol L^{-1} potassium iodide (KI) solution and 0.5 ml of 0.1mol L^{-1} potassium hydrogen phthalate ($C_8H_5KO_4$) solution were added to 1 ml obtained solution and kept for 30min. H_2O_2 reacted with I^- under acidic conditions to form I_3^- ($H_2O_2 + 3I^- + 2H^+ \rightarrow I_3^- + 2H_2O$), which has a strong absorption at about 350 nm. The content of I_3^- was determined by measuring the absorbance at 350 nm by UV–vis spectroscopy, from which the total amount of H_2O_2 produced during the reaction can be calculated. **Figure S24** shows the standard curve of H_2O_2 and the raw data of the UV-vis absorption spectrum of H_2O_2 generated by Nv-C≡N-CN in pure water under visible light ($\lambda \geq 420$ nm).

The apparent quantum yield (AQY) of H_2O_2 formed on Nv-C≡N-CN under the conditions of pure water and sacrificial agent were tested separately. The AQY test used a 300 W Xe lamp with different bandpass filters of 400, 420, 450, 500, and 550 nm (FWHM=15 nm). The concentration of the photocatalyst in the reaction solution was

still 1 g L^{-1}. The irradiation area was controlled to 1.69 cm^2 and the optical power meter (Thorlabs) determined the average light intensity. The AQY was calculated by the following formula:

$$AQY = \frac{2 \times H_2O_2 \text{ formed (mol)}}{\text{the number of incident photons (mol)}} \times 100\%$$

The solar-to-chemical conversion efficiency test was carried out with the photocatalyst in pure water (1g L^{-1}) and AM 1.5G light source. The solar-to-chemical conversion (SCC) efficiency is determined by the following formula:

$$SCC = \frac{[\Delta G_{H_2O_2}] \times [n_{H_2O_2}]}{I \times S \times T} \times 100\%$$

where $\Delta G_{H_2O_2}$, $n_{H_2O_2}$, I, S, and T represent the free energy for H_2O_2 generation (117 KJ mol^{-1}), the molar amount of H_2O_2 generated, the energy intensity of the AM 1.5G solar irradiation (100 mW cm^{-2}), the irradiated sample area and the irradiation time (s), respectively.

1.5. Photocatalytic oxygen generation

The photocatalytic oxygen generation reaction was tested in a Pyrex top-irradiated reaction vessel under visible light irradiation and the reactor was connected to the PerfectLight glass enclosed gas system (Labsolar-6A). 30 mg of photocatalyst was dispersed in 30 ml of pure water. After that, $AgNO_3$ (20 mM) was added to the reaction solution as an electron acceptor, and La_2O_3 (30 mg) was added to maintain the pH of the reaction solution. N_2 was passed into the reactor for 30 minutes to remove residual gas. The photocatalytic O_2 generation was performed under the visible light irradiation ($\lambda \geq 420$ nm) of a 300W xenon lamp. The generated O_2 was detected by an online gas chromatograph (5Å molecular sieve column, Ar carrier).

1.6. Electrochemical measurement of oxygen reduction reaction (ORR)

Rotating ring-disk electrode (RRDE) was used to measure the number of transferred electrons (n) and H_2O_2 selectivity of the sample in the ORR reaction. The electrochemical measurement used a three-electrode system, in which RRDE was the working electrode, Ag/AgCl was the reference electrode, and Pt/C was the counter electrode. And O_2-saturated 0.1M KOH solution as electrolyte. The speed of RRDE was set to 1600 rpm and the potential range was set to 0-1.0 V vs. RHE. The catalyst ink on the RRDE working electrode is prepared as follows. 4 mg of the catalyst was fully ground and placed in 300 μL of pure water, 700 μL of isopropanol, and 10 μL of Nafion solution (4%) for ultrasonic dispersion for 1 h. Next, 10 μL of ink was dropped on the RRDE electrode and dried at room temperature (the catalyst loading was approximately 0.161 mg cm^{-2}).

The number of transferred electrons (n) is calculated according to the following formula:

$$n = \frac{I_d}{I_d + I_r/N} \times 100\%$$

The selectivity of H_2O_2 is calculated according to the following formula:

$$H_2O_2(\%) = \frac{I_r/N}{I_d + I_r/N} \times 100\%$$

Where I_r is the ring current, I_d is the disc current, and N is the collection efficiency (N=0.37).

2. Computational methods

We have employed the Vienna Ab Initio Package (VASP) to perform all the density functional theory (DFT) calculations within the generalized gradient approximation (GGA) using the PBE formulation. We have chosen the projected augmented wave (PAW) potentials to describe the ionic cores and take valence electrons into account using a plane wave basis set with a kinetic energy cutoff of 400 eV. Partial occupancies of the Kohn−Sham orbitals were allowed using the Gaussian smearing method and a width of 0.05 eV. The electronic energy was considered self-consistent when the energy change was smaller than 10^{-5} eV. A geometry optimization was considered convergent when the force change was smaller than 0.02 eV/Å. Grimme's DFT-D3 methodology was used to describe the dispersion interactions.

The equilibrium lattice constants of rectangular g-C_3N_4 monolayer unit cell were optimized, when put in a vacuum in the depth of 20 Å and using a 9×5×3 Monkhorst-Pack k-point grid for Brillouin zone sampling, to be a=7.136 Å, b=12.359 Å. We then use it to construct a Y-direction-edged g-C_3N_4 monolayer model with p (2×1) periodicity in the x and y directions and 2 stoichiometric layers in the z direction separated by a vacuum layer in the depth of 20 Å in order to separate the surface slab from its periodic duplicates. The unsaturated N atoms on the edge are saturated by H atoms. During structural optimizations, the gamma point in the Brillouin zone was used for k-point sampling, and all atoms were allowed to relax.
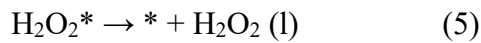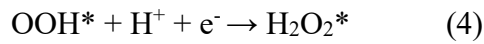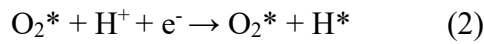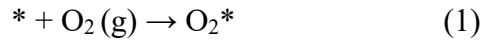
The adsorption energy (E_{ads}) of adsorbate A was defined as

$$E_{ads} = E_{A/surf} - E_{surf} - E_{A(g)}$$

where $E_{A/surf}$, E_{surf} and $E_{A(g)}$ are the energy of adsorbate A adsorbed on the surface, the energy of clean surface, and the energy of isolated A molecule in a cubic periodic box with a side length of 20 Å and a 1×1×1 Monkhorst-Pack k-point grid for Brillouin zone sampling, respectively.

The free energy of a gas phase molecule or an adsorbate on the surface was calculated by the equation $G = E + ZPE - TS$, where E is the total energy, ZPE is the zero-point energy, T is the temperature in kelvin (298.15 K is set here), and S is the entropy.

The process of 2e⁻ ORR proceeds as the following equation:

$$* + O_2\,(g) \rightarrow O_2* \qquad\qquad (1)$$

$$O_2* + H^+ + e^- \rightarrow O_2* + H* \qquad (2)$$

$$O_2* + H* \rightarrow OOH* \qquad\qquad (3)$$

$$OOH* + H^+ + e^- \rightarrow H_2O_2* \qquad (4)$$

$$H_2O_2* \rightarrow * + H_2O_2\,(l) \qquad\qquad (5)$$

Where * represents the surface-active site.

The N_{2C} vacancy formation energy of N_{V-X}-C≡N-CN (x=1, 2, 3, 4, 5, 6) is calculated by the following formula:

$$E_f = E_{(N2C)} + E_{(N\ atom)} - E_{original\text{-}C≡N\text{-}CN}$$

where E_f is the N_{2C} vacancy formation energy; $E_{(N2C)}$ is the energy of an N_{2C} vacancy in C≡N-CN structure; $E_{original\text{-}C≡N\text{-}CN}$ is the total energy of the original C≡N-CN (-519.76 eV); $E_{(N\ atom)}$ is the energy of one N atom taking into account the spin effect (-3.12 eV).

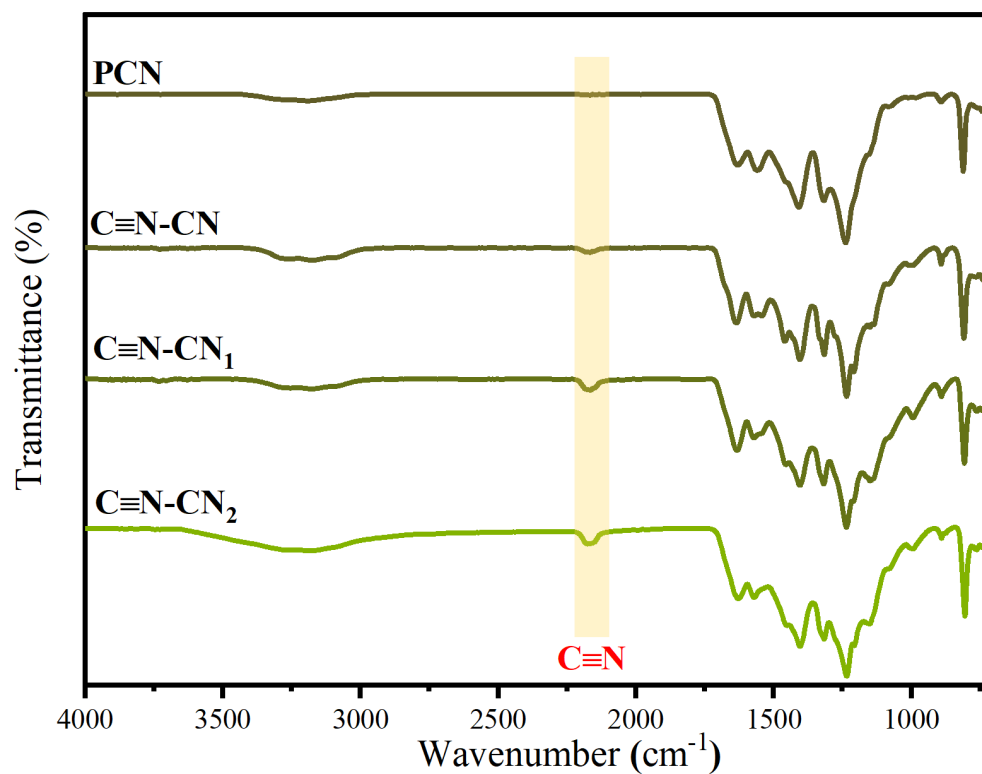## 3. Results and discussion (Fig. S1-24 and Table S1-9)

3.1 Fig. S1-S24:

Fig. S1 FTIR transmission spectra of PCN, C≡N-CN, C≡N-CN$_1$, and C≡N-CN$_2$.

The ratios of urea to thiourea in the precursors of C≡N-CN, C≡N-CN$_1$, and C≡N-CN$_2$ are 1:1, 1:2, and 1:3, respectively.
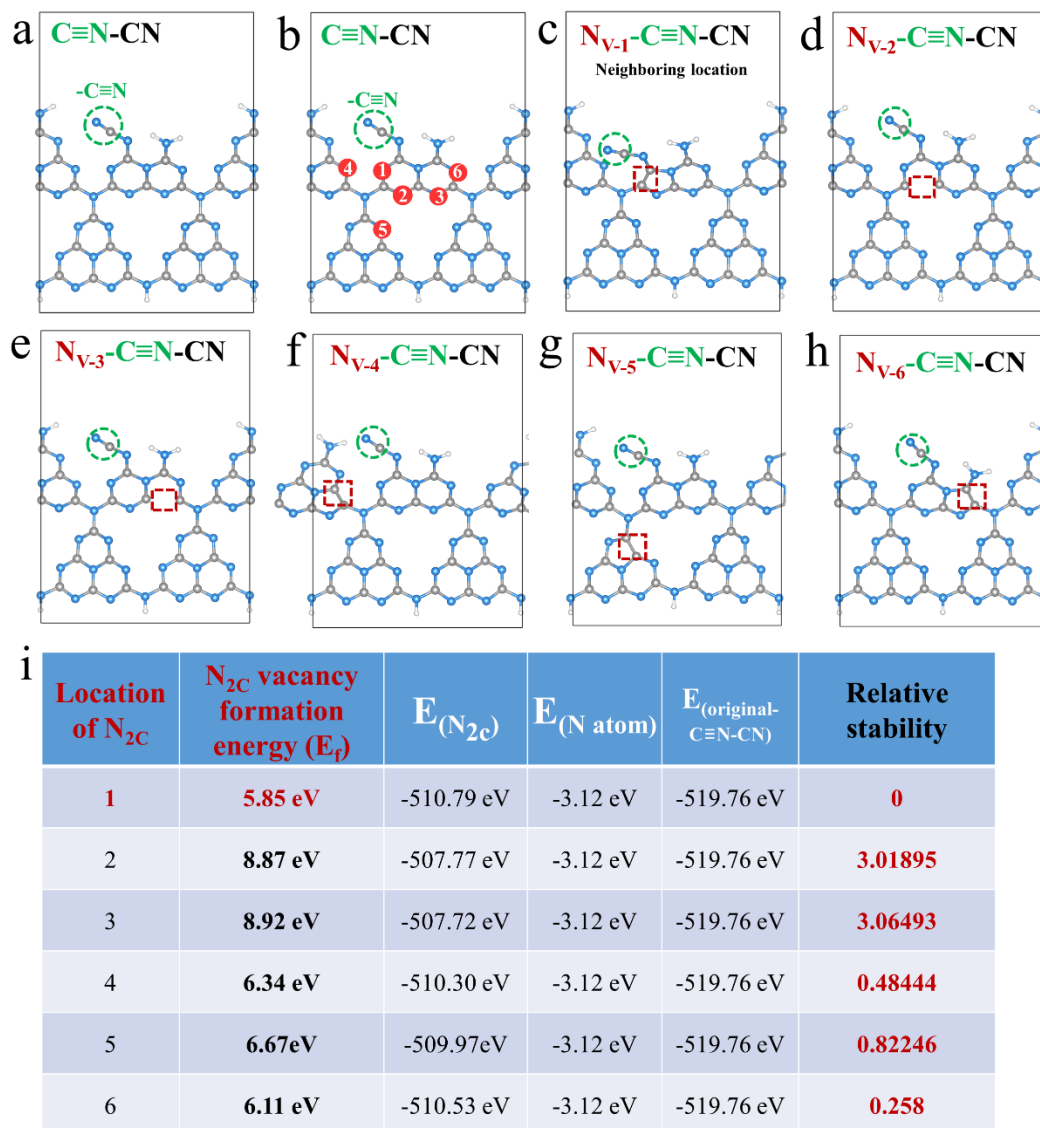
Fig. S2 (a) The structural model of C≡N-CN. (b) 6 types of N_{2C} positions selected on C≡N-CN. (c-h) 6 kinds of N_{V-X}-C≡N-CN (x=1, 2, 3, 4, 5, 6) with different relative positions of -C≡N group and N_{2C} vacancy after structural optimization. (i) The formation energy of N_{2C} vacancies in different positions on C≡N-CN (including original data).

Fig. S2a and Fig. S2b are respectively represented as C≡N-CN and 6 types of selected N_{2C} atoms at different positions from the -C≡N group on C≡N-CN. After that, we successively created these N_{2C} vacancies (6 types) at different positions relative to the

Location of N_{2C}	N_{2C} vacancy formation energy (E_f)	$E_{(N_{2c})}$	$E_{(N\ atom)}$	$E_{(original-C≡N-CN)}$	Relative stability
1	5.85 eV	-510.79 eV	-3.12 eV	-519.76 eV	0
2	8.87 eV	-507.77 eV	-3.12 eV	-519.76 eV	3.01895
3	8.92 eV	-507.72 eV	-3.12 eV	-519.76 eV	3.06493
4	6.34 eV	-510.30 eV	-3.12 eV	-519.76 eV	0.48444
5	6.67eV	-509.97eV	-3.12 eV	-519.76 eV	0.82246
6	6.11 eV	-510.53 eV	-3.12 eV	-519.76 eV	0.258

-C≡N group on C≡N-CN, and calculated these N_{2C} vacancies formation energy (Fig. S2i). In Fig. S2c-h, the 6 models after structural optimization are represented as dual defect sites g-C_3N_4 with different relative positions of -C≡N group and N vacancy, and they are named as N_{V-X}-C≡N-CN in turn (X=1, 2, 3, 4, 5, 6). The calculation results and the original data are shown in Fig. S2i, among the 6 models, the N_{2C} vacancy formation energy on N_{V-1}-C≡N-CN is the lowest, corresponding to the nearest neighbors of the -C≡N group and the N_{2C} vacancy. In order to compare the relative stability, we set the total energy of the N_{V-1}-C≡N-CN system as 0. Subtracting N_{V-1}-C≡N-CN from the N_{2C} vacancy formation energies of the other 5 models (N_{V-2-6}-C≡N-CN), it is found that these energies are all positive values (Fig. S2i). This shows that the -C≡N group and N vacancy in the nearest neighbor location are more stable than other positions. According to the principle of least energy, this indicates that the N_{2C} vacancy closest to the -C≡N group is easier to form, and such a neighboring location should be more stable. Therefore, the nearest neighbor of -C≡N groups and N_{2C} vacancies in N_V-C≡N-CN was determined (Fig. S2c).
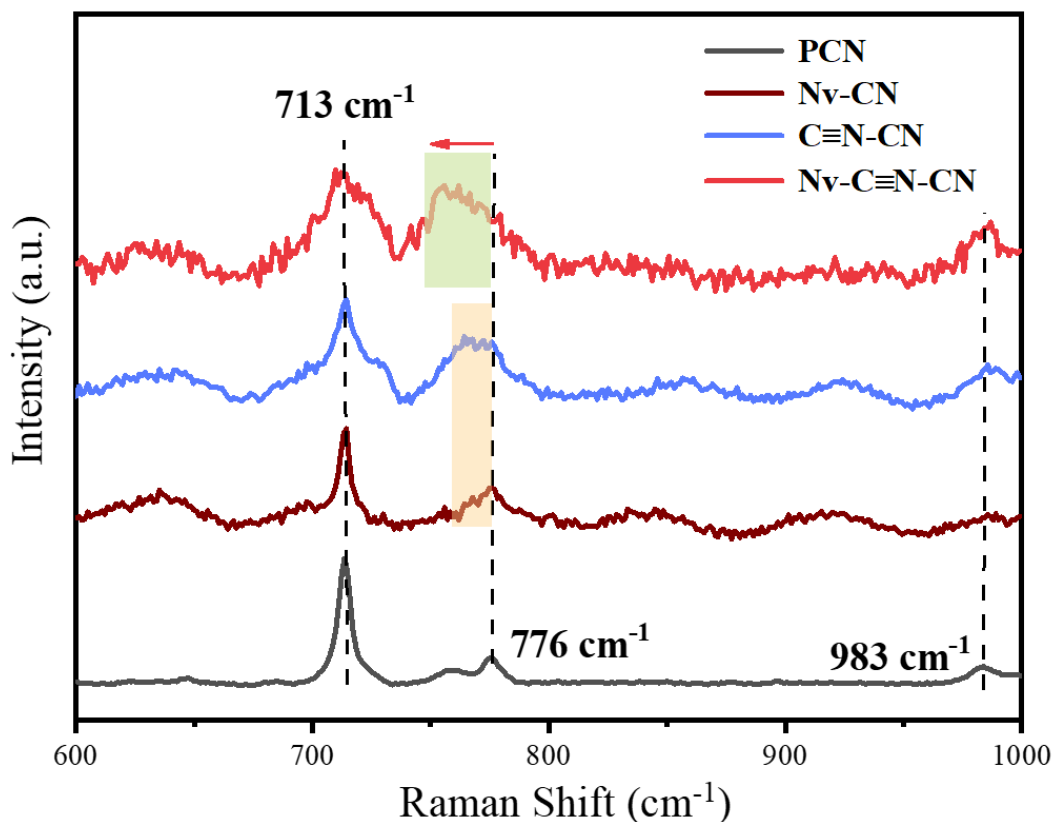
Fig. S3 Raman spectra of PCN, C≡N-CN, Nv-CN, and Nv-C≡N-CN (laser wavelength: 785 nm; power: 0.5 mW; lens: 50 objective; acquisition time: 10 s).

In **Fig. S3**, the Raman characteristic peaks of the samples are consistent with that reported in the literature.[2] Compared with PCN, the characteristic peak intensity of Nv-CN at 776 cm^{-1} is enhanced, which might be the structure change of heptazine caused by the N vacancies. Simultaneously, the Raman peak of C≡N-CN has a slight blue shift. This could be attributed to the structural change caused by the -C≡N groups, which is also related to the increased -C≡N ratio in XPS (**Fig. 2d**). It is worth noting that Nv-C≡N-CN has a larger change, which is manifested as a significant enhancement of the characteristic peak at 755 cm^{-1} and an obvious blue shift (from 776 cm^{-1} to 755 cm^{-1}). From PCN to Nv-C≡N-CN, I_{776}/I_{713} (Raman peak intensity comparison) in the samples gradually increased, indicating that the accumulated defects have caused changes in the

structure. Furthermore, compared with the single sharp Raman peak of PCN at 776 cm^{-1}, with the introduction of -C≡N groups and N vacancies, the Raman peak at about 776 cm^{-1} of other samples becomes multimodal vibration (Nv-C≡N-CN is the most obvious). This may be the influence of neighboring -C≡N groups and N vacancies on the structure.
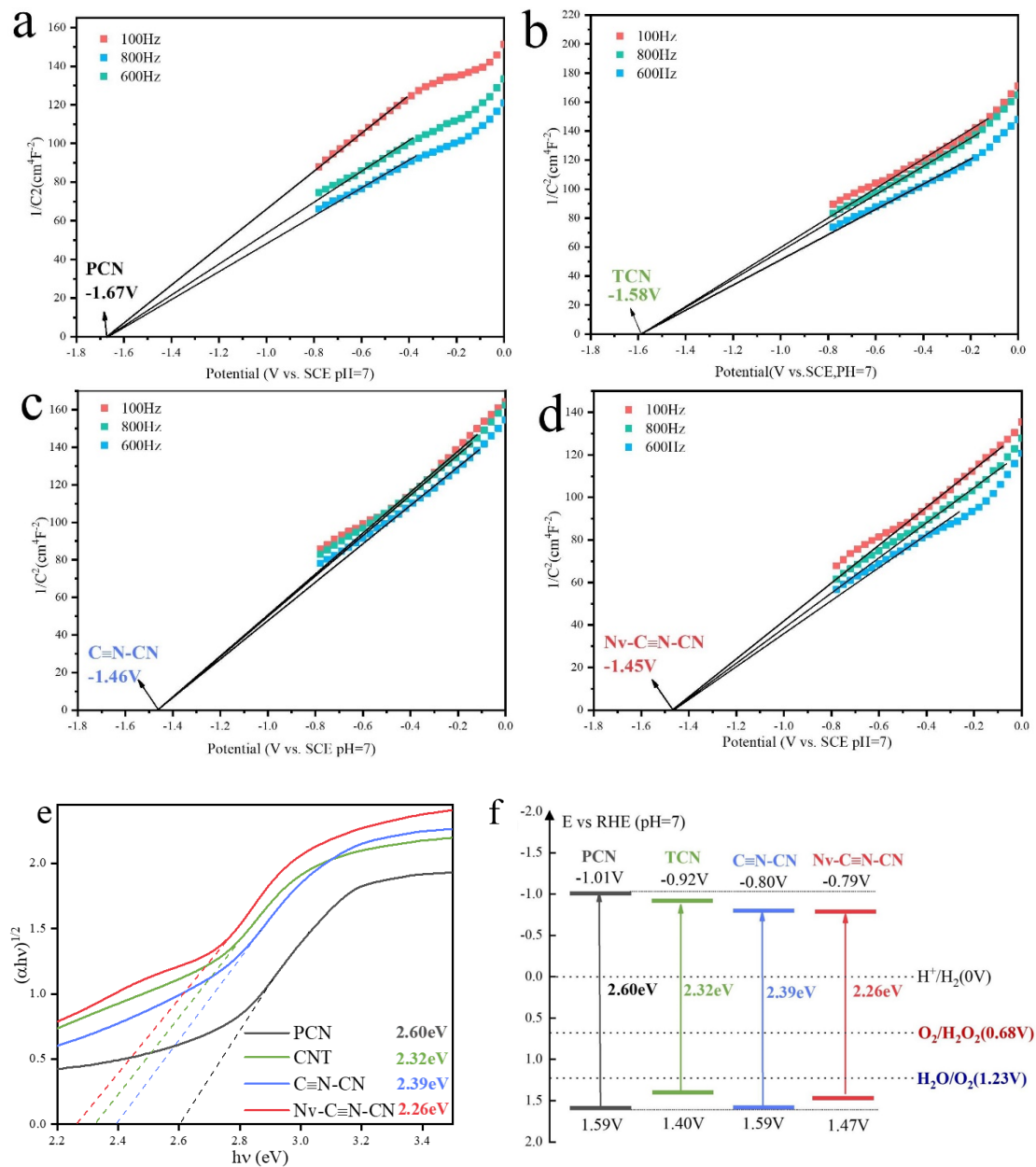
Fig. S4 Mott-Schottky plots of (a) PCN, (b) TCN, (c) C≡N-CN, and (d) Nv-C≡N-CN.

(e) Plots of transformed Kubelka-Munk function versus photon energy of all samples.

(f) The schematic diagram of the band gap positions of the samples.
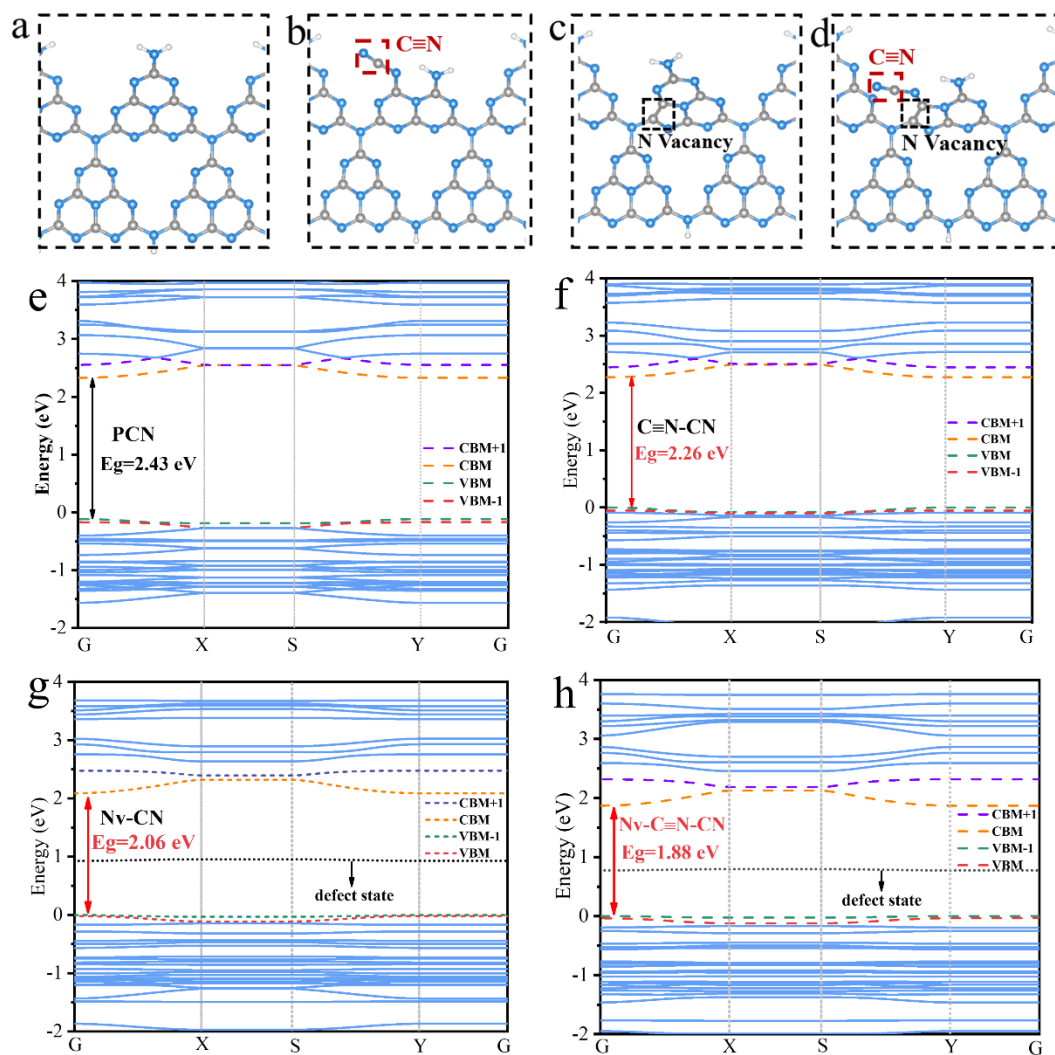
Fig. S5 (a-d) The structural model of the four types of defect g-C_3N_4 (PCN, C≡N-CN, Nv-CN, and Nv-C≡N-CN) and the corresponding (e-h) calculated band structure.

As shown in **Fig. S5b-c**, a -C≡N group and an N_{2C} vacancy is introduced into the g-C_3N_4 unit cell, respectively, and the bandgap energy of C≡N-CN and Nv-CN is calculated. As shown in **Fig. S5e-g**, after the introduction of a -C≡N group and an N vacancy, the band gap of PCN decreased from 2.43 eV to 2.26 eV (C≡N-CN) and 2.06 eV (Nv-CN), respectively, indicating that both -C≡N groups and N vacancies can narrow the band gap. However, the introduction of -C≡N groups does not cause the

appearance of defect levels (**Fig. S5f**). The introduction of N vacancies brings defect levels (**Fig. S5g**). When the -C≡N group and the N vacancy coexist in the structure of g-C$_3$N$_4$, the band gap is reduced from 2.43 eV to 1.88 eV, indicating that the -C≡N groups and the N vacancies cooperate to narrow the band gap.

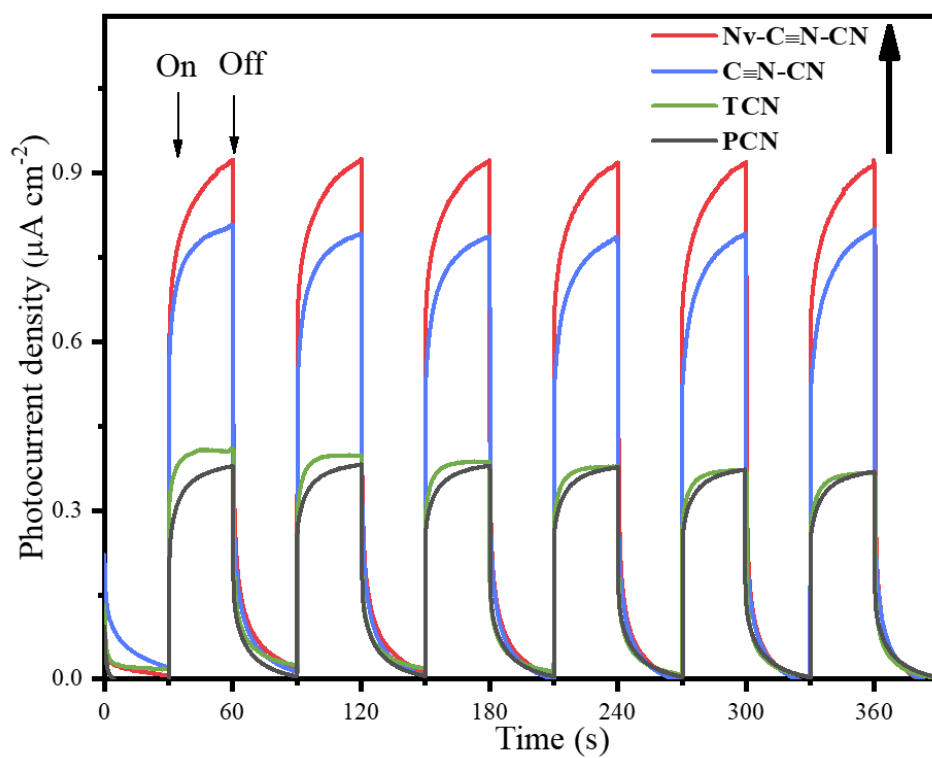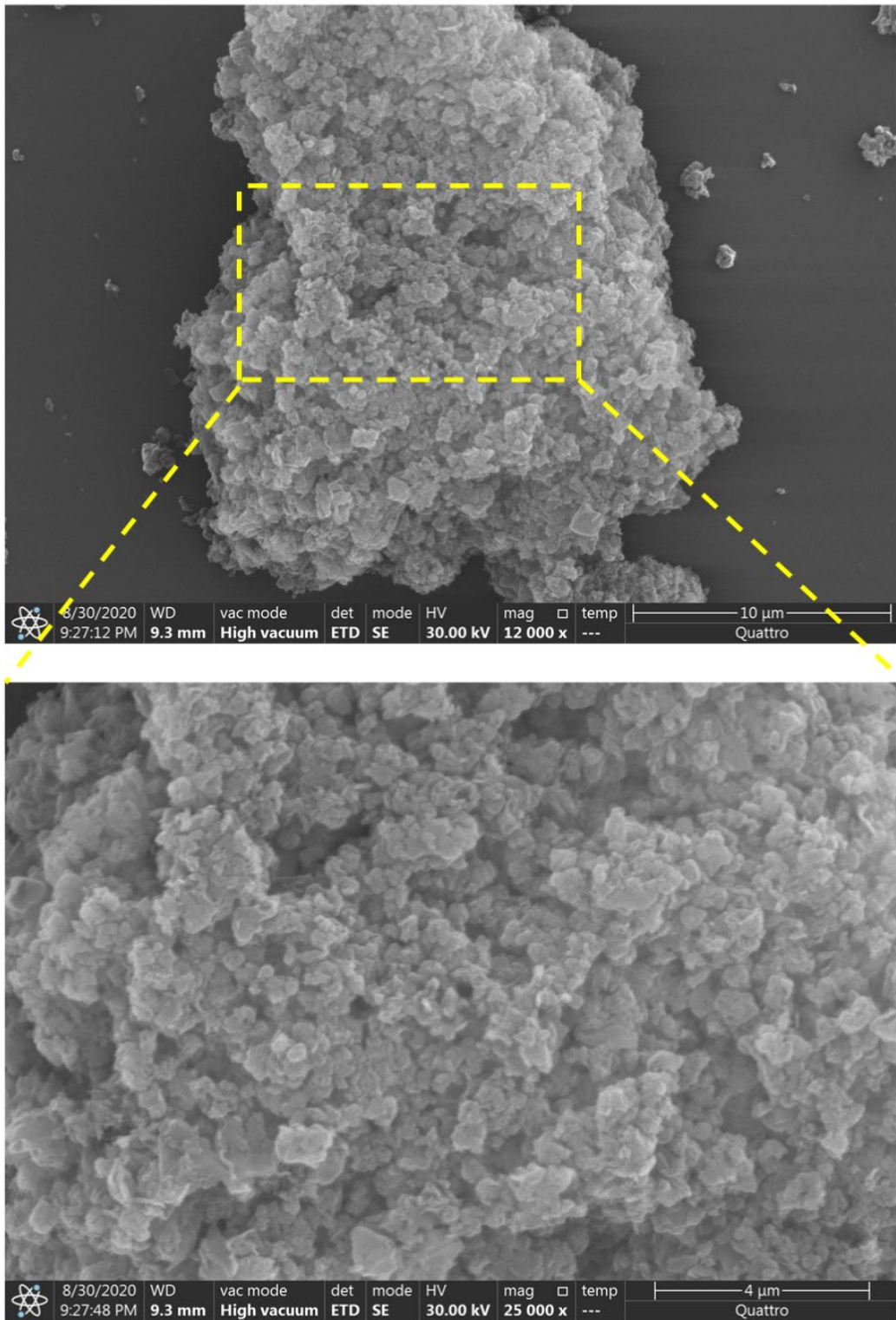**Fig. S6** Transient photocurrent response (TPR) of all samples.

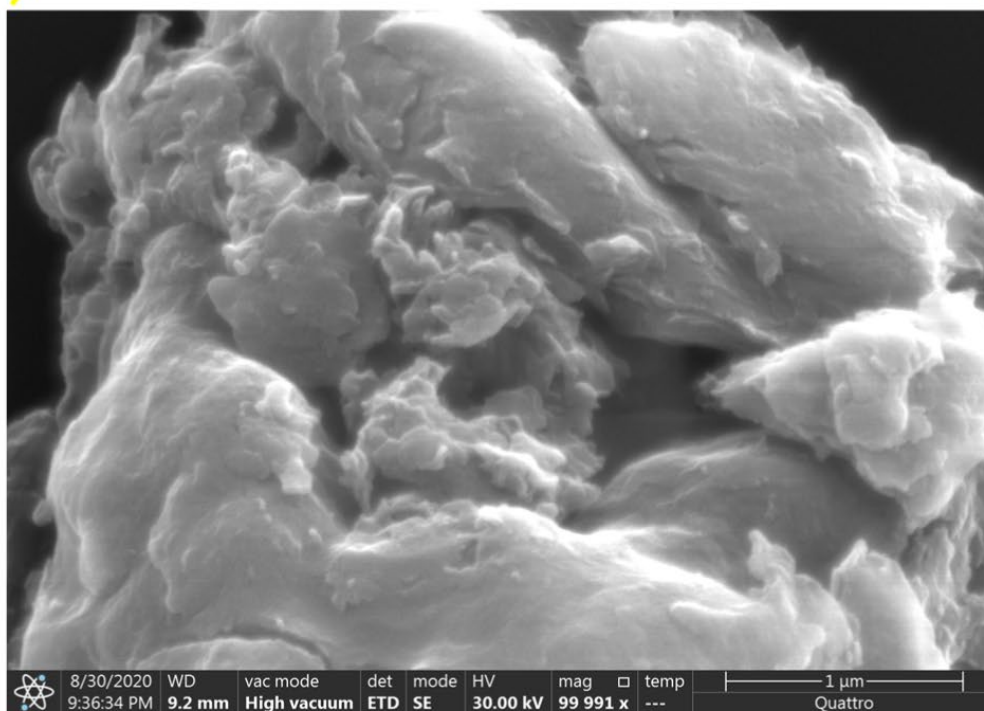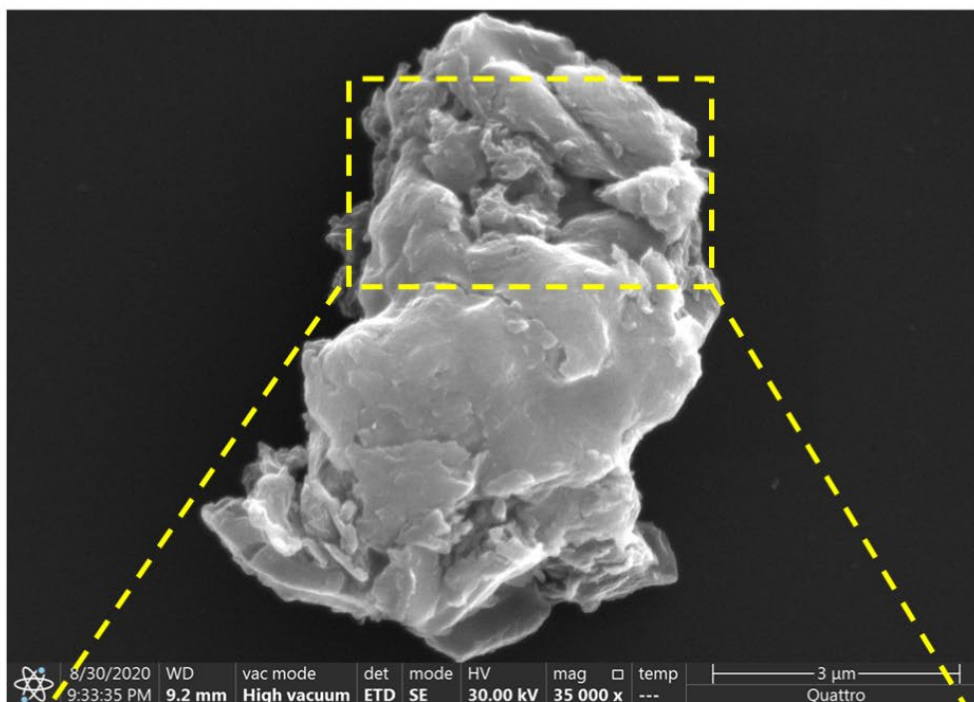**Fig. S7** SEM images of PCN under different magnifications.

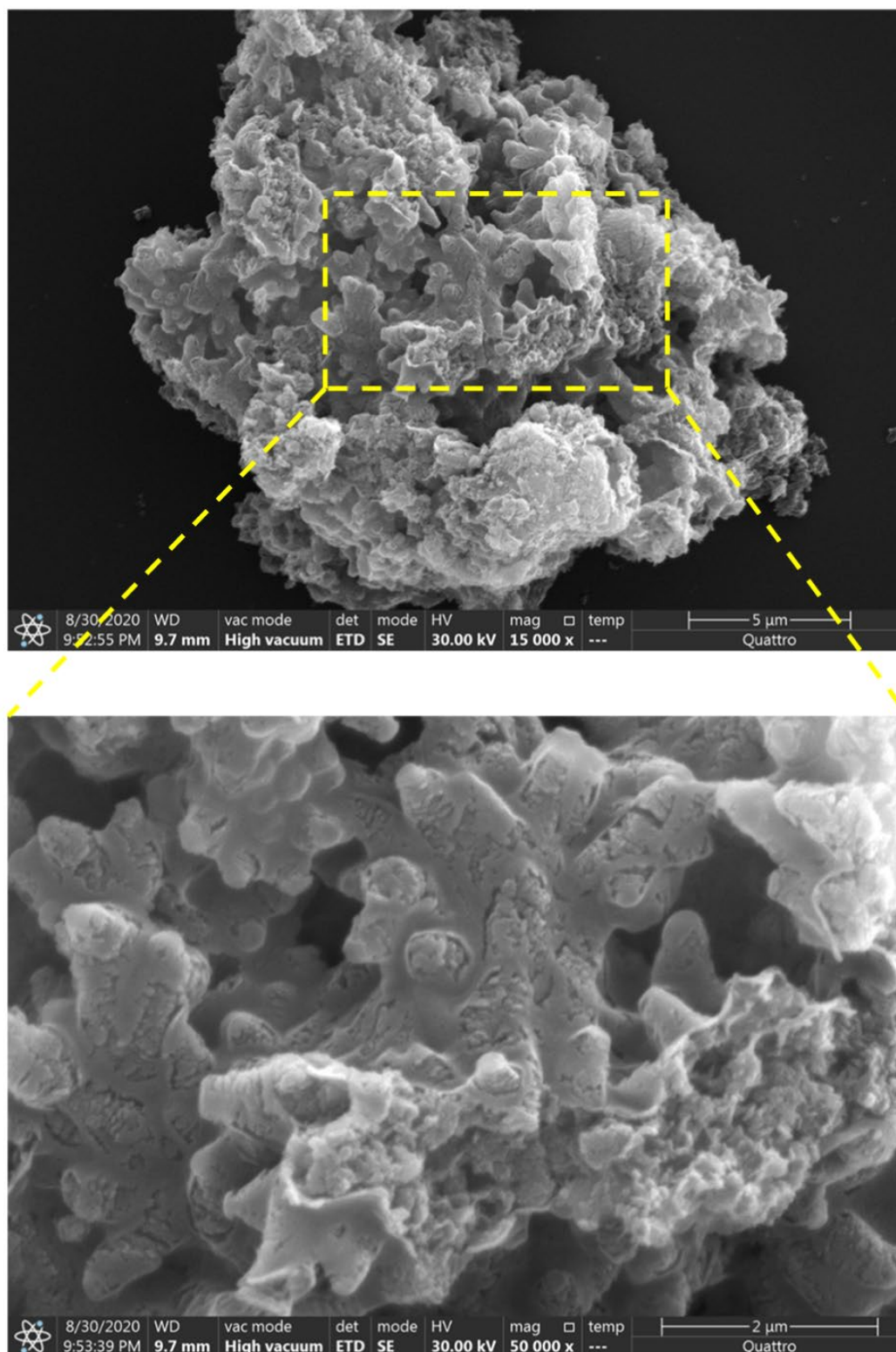**Fig. S8** SEM images of TCN under different magnifications.

Fig. S9 SEM images of C≡N-CN under different magnifications.
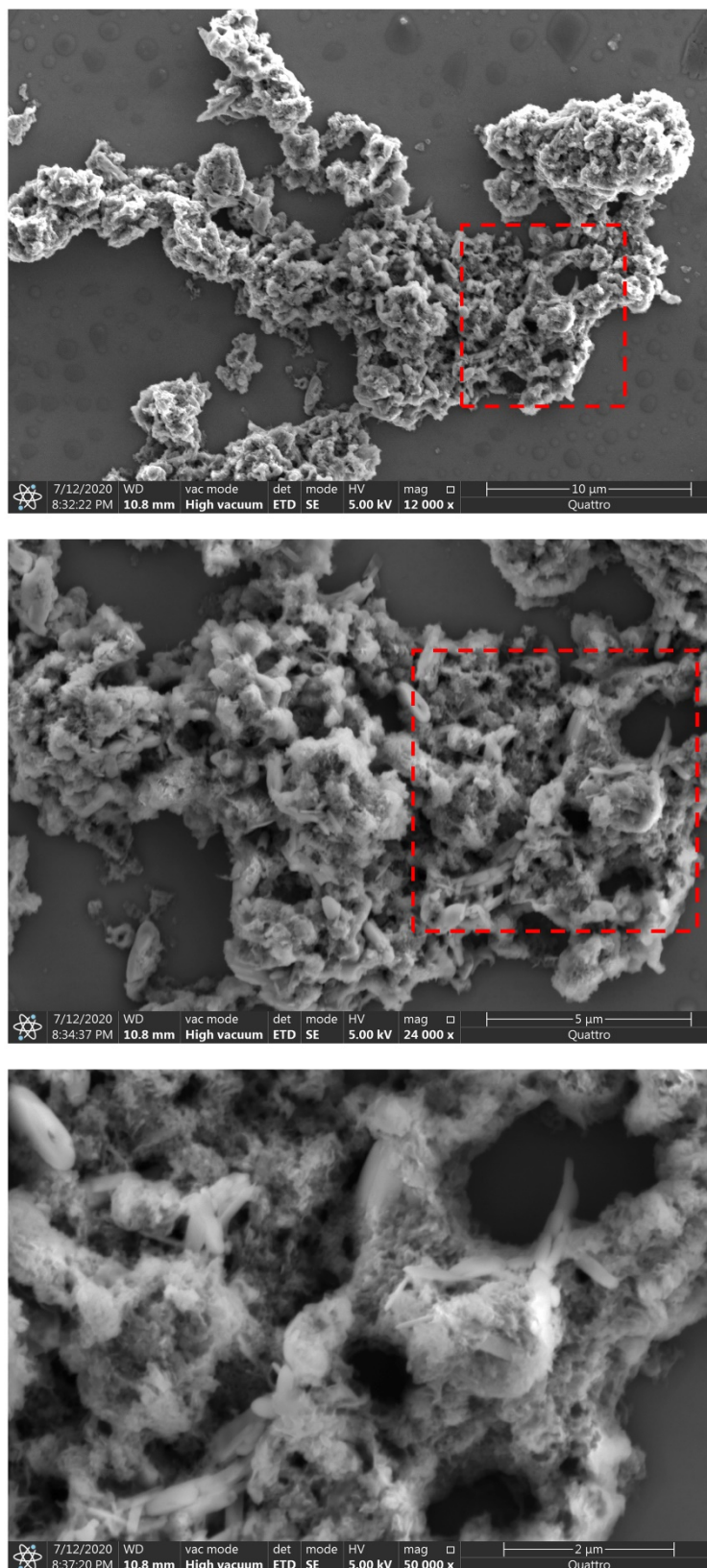
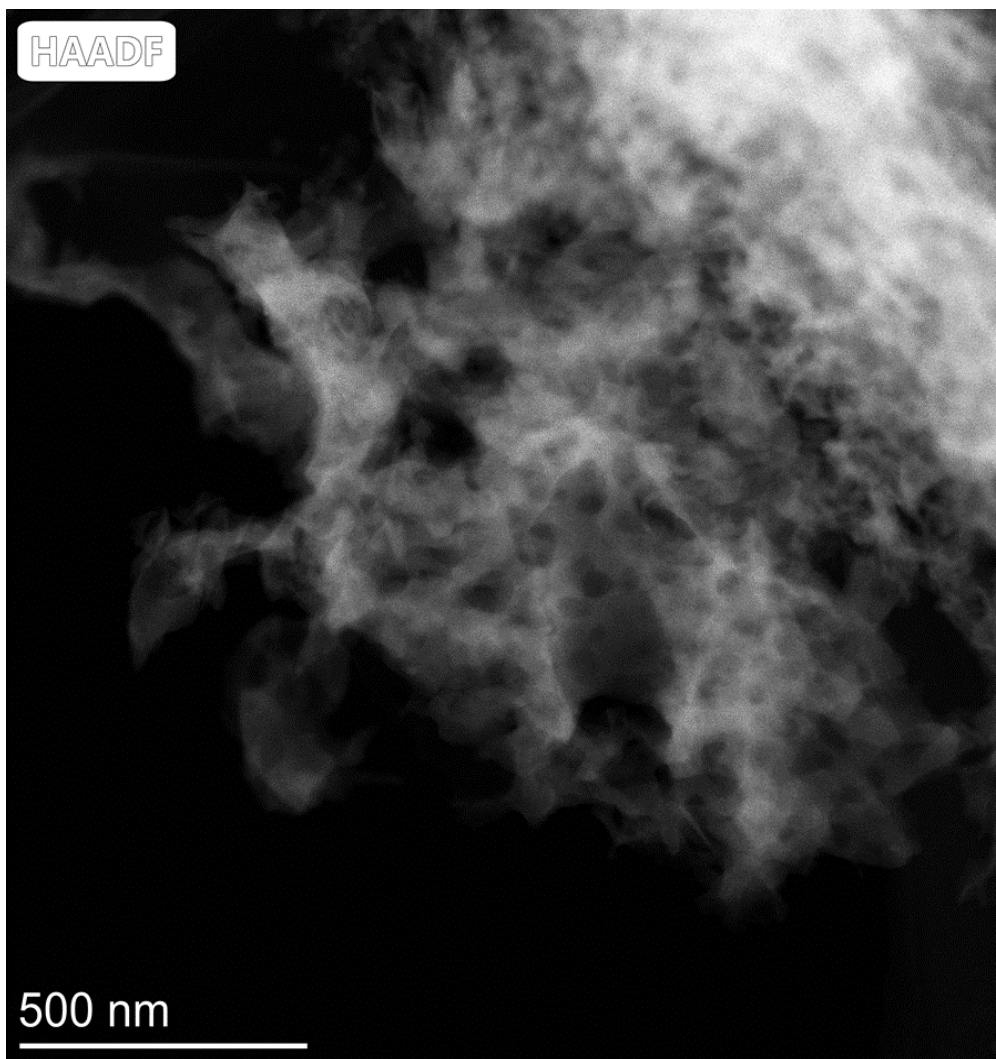**Fig. S10** SEM images of Nv-C≡N-CN under different magnifications.
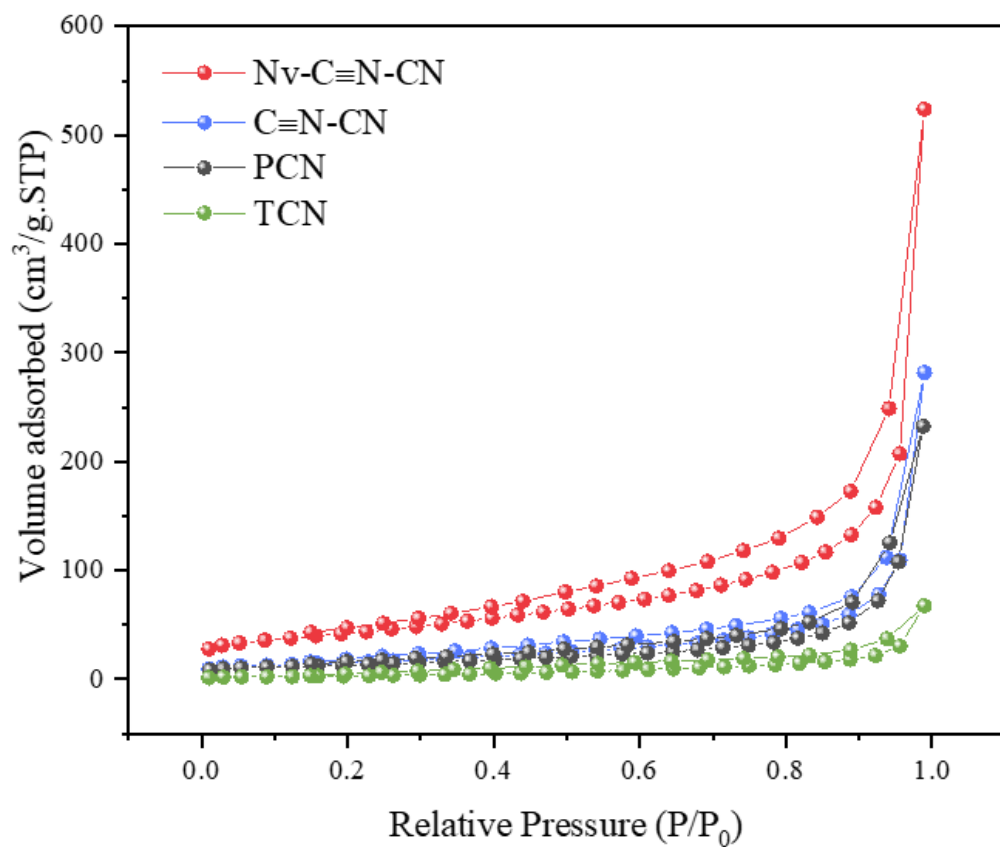
Fig. S11 TEM image of Nv-C≡N-CN.

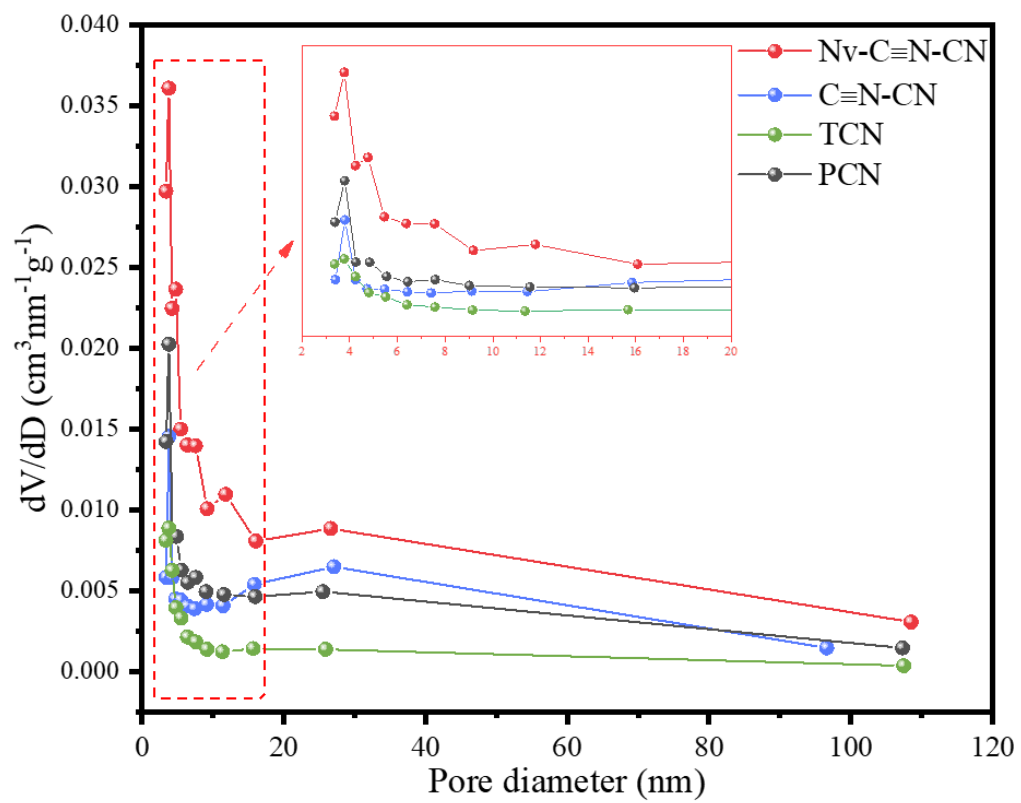**Fig. S12** N_2 adsorption-desorption isotherms for PCN, TCN, C≡N-CN, and Nv-C≡N-CN.

Fig. S13 Pore size distribution curves for PCN, TCN, C≡N-CN, and Nv-C≡N-CN.
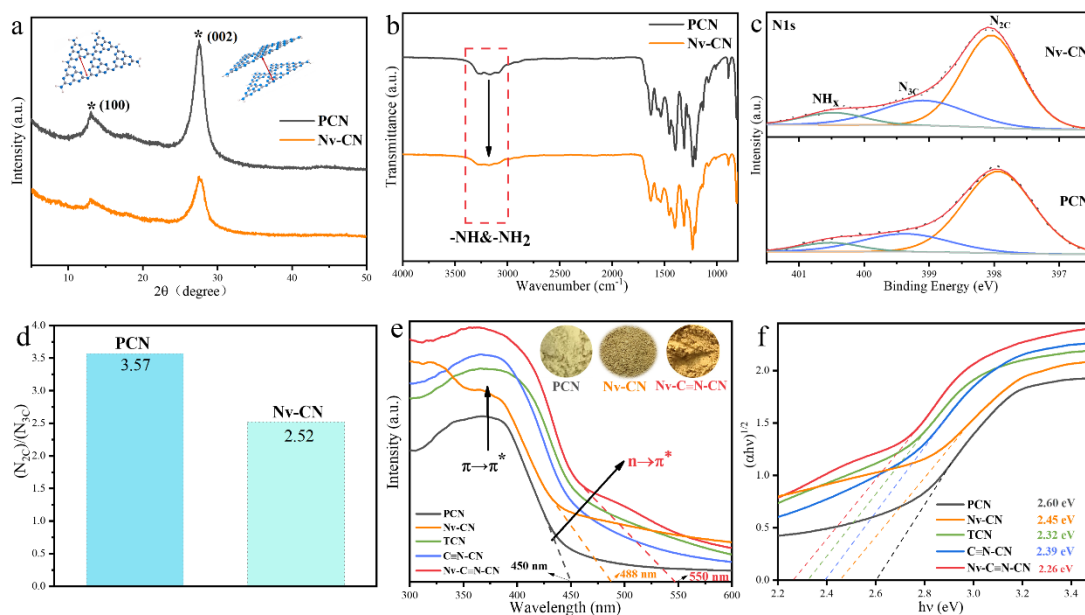
Fig. S14 (a) XRD patterns and (b) FTIR spectra, and (c) N1s XPS spectra of PCN and Nv-CN. (d) The atomic ratio of N_{2C}/N_{3C} between PCN and Nv-CN calculated by N1s XPS spectra. (e)UV-vis DRS (the illustrations in **Fig. S14e** represent the colors of different samples) and (b) plots of transformed Kubelka-Munk function versus photon energy of all samples.

In **Fig. 2** of the manuscript and the corresponding discussion, it has been proved in detail that high-temperature etching of g-C_3N_4 in an argon atmosphere leads to the appearance of N_{2C} vacancies in the structure. Similarly, in **Fig. S14a**, compared with PCN, the two characteristic peaks of Nv-CN are weakened after high temperature etching. It shows that the argon treatment weakens the interlayer accumulation and affects the structural unit of g-C_3N_4. In FTIR (**Fig. S14b**), compared to PCN, the N-H bond stretching vibration of Nv-CN was slightly weaker, indicating that argon thermal

etching reduces the concentration of N-H bonds. Comparing the N1s of PCN and Nv-CN, it was found that the surface atomic ratio of N_{2C}/N_{3C} decreased from 3.57 to 2.52, which also proved the appearance of N_{2C} vacancies. The above characterization comprehensively proves the appearance of N_{2C} vacancies in Nv-CN, and it is in line with current literature reports.[3, 4]

In **Fig. S14e**, after high temperature argon etching, the color of the sample changed from light yellow (PCN) to dark yellow (Nv-CN), and the red shift of the absorption edge can be clearly seen. This shows that the appearance of N vacancies expands the absorption range of visible light (from 450 nm of PCN to 488 nm of Nv-CN) and enhances the light absorption capacity. As shown in **Fig. S14e**, it is worth noting that Nv-CN has an obvious extended absorption tail, which is attributed to the n-π* electronic transition caused by the lone pair of electrons at the N vacancies defect sites. Meanwhile, in **Fig. S14f**, the bandgap of PCN was narrowed from 2.60 eV to 2.45 eV of Nv-CN, indicating that the N vacancies can narrow the bandgap and adjust the band structure.
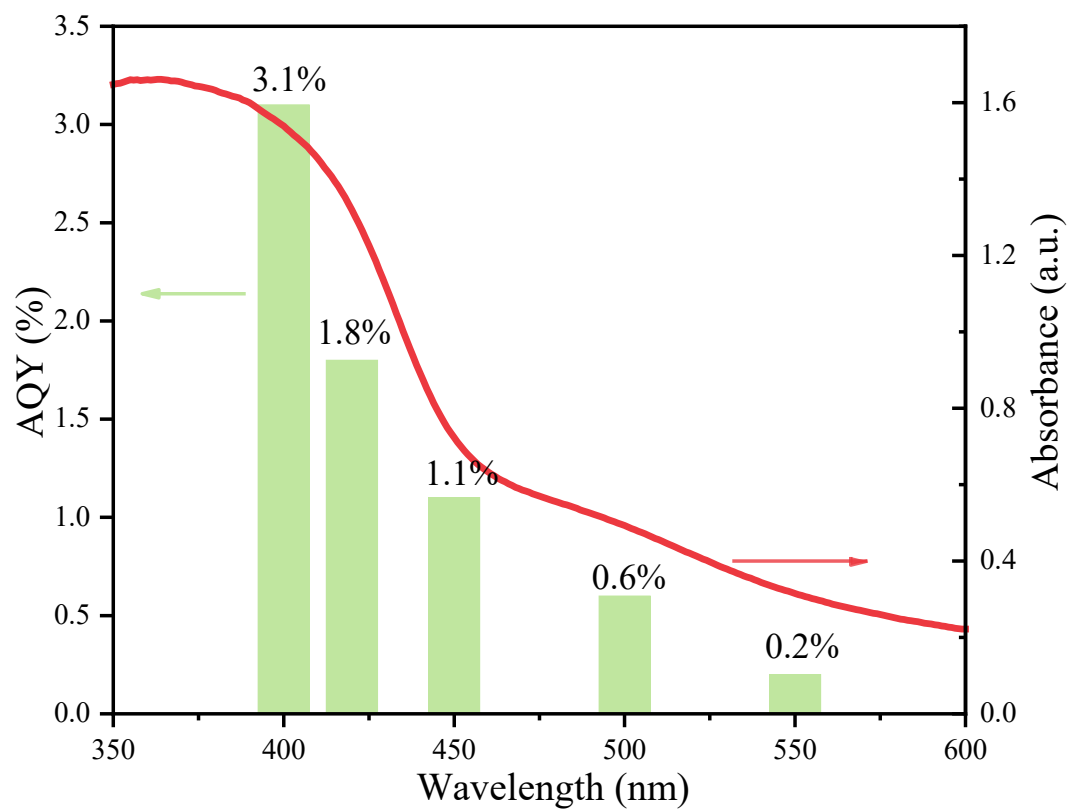
Fig. S15 The wavelength-dependent AQY for photocatalytic H_2O_2 generation by Nv-C≡N-CN (Conditions: $λ ≥ 420$ nm; pure water, pH=7;1 g L^{-1} catalyst).
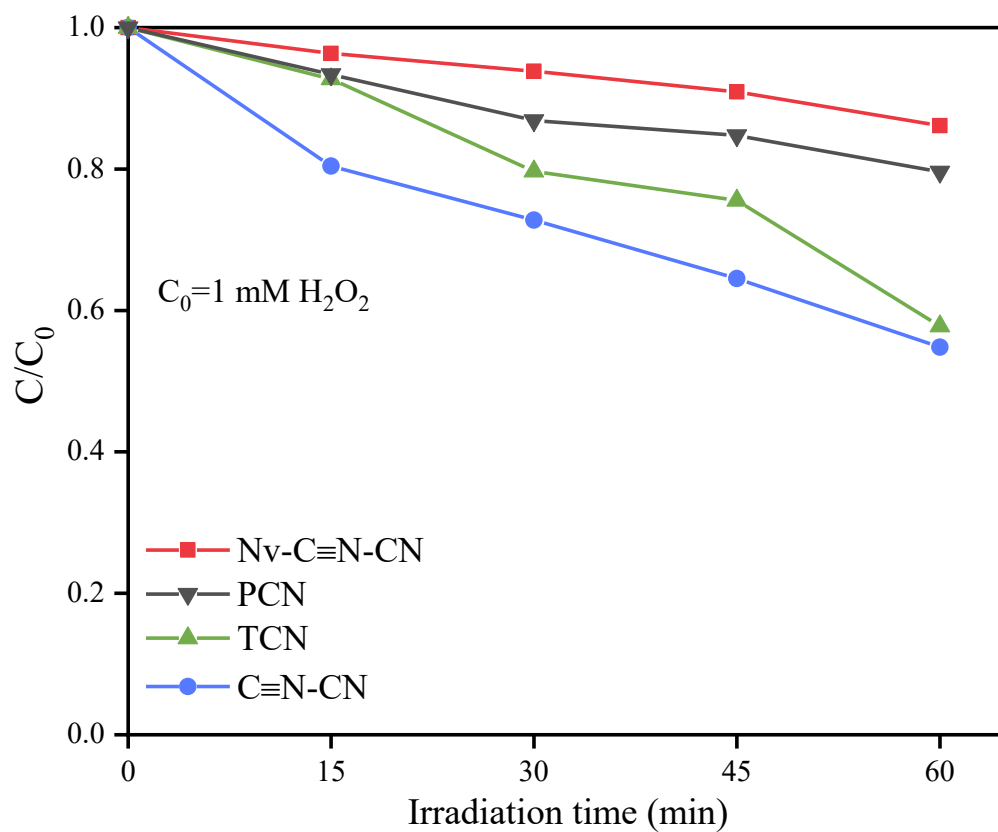
Fig. S16 Photocatalytic decomposition of H_2O_2 (1 mM) on different samples under visible light irradiation ($\lambda \geq 420$ nm, 1 g L^{-1} catalyst).
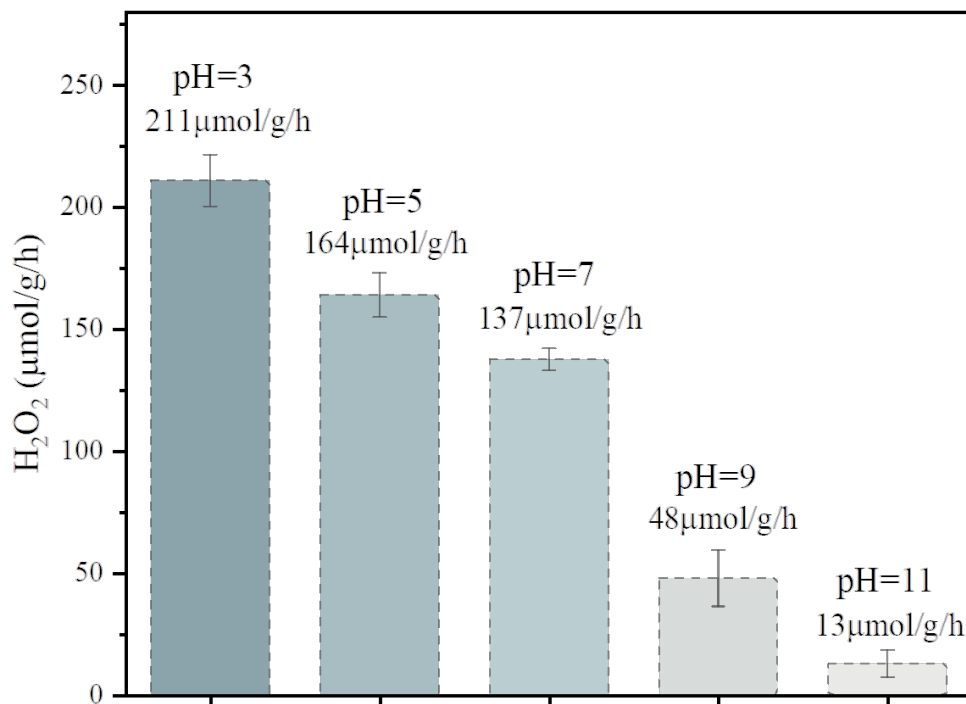
Fig. S17 The influence of different pH in the reaction system on the photocatalytic

H_2O_2 generation rate of Nv-C≡N-CN. Conditions: $\lambda \geq 420$ nm, 1 g L^{-1} catalyst.
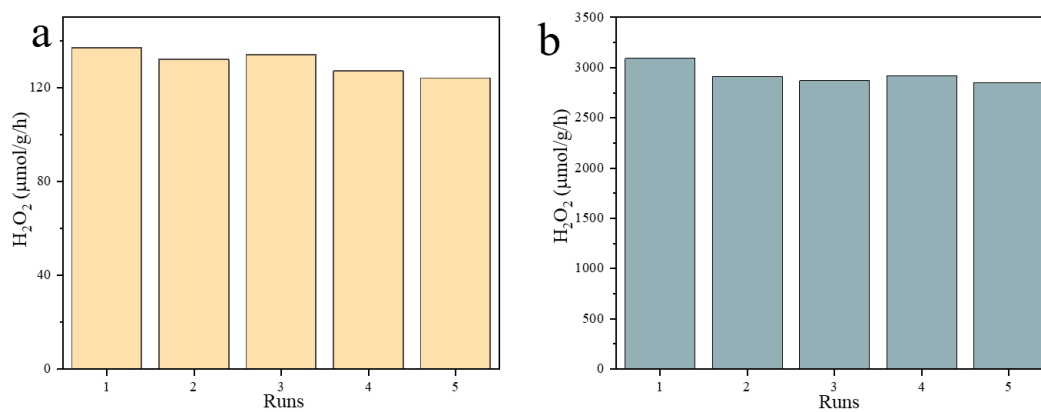
Fig. S18 Cyclic test of photocatalytic H_2O_2 generation over Nv-C≡N-CN in (a) pure

water (pH=7) and (b) sacrificial agent conditions (10% IPA, pH=3).
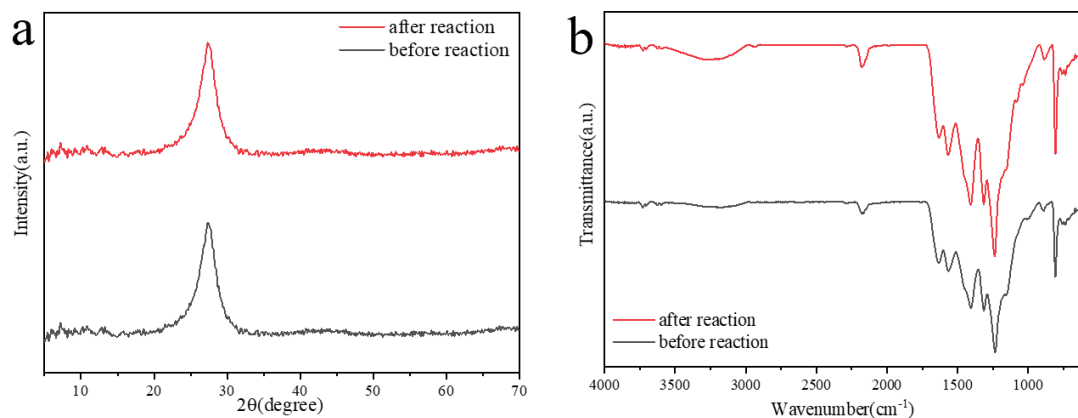
Fig. S19 (a) XRD and (b) FTIR spectrum of Nv-C≡N-CN after the photocatalytic reaction.

As shown in **Fig. S19**, there is no obvious change in XRD and FTIR spectra of Nv-C≡N-CN before and after the photocatalytic reaction, which indicates that Nv-C≡N-CN has good stability in the photocatalytic H_2O_2 generation reaction.
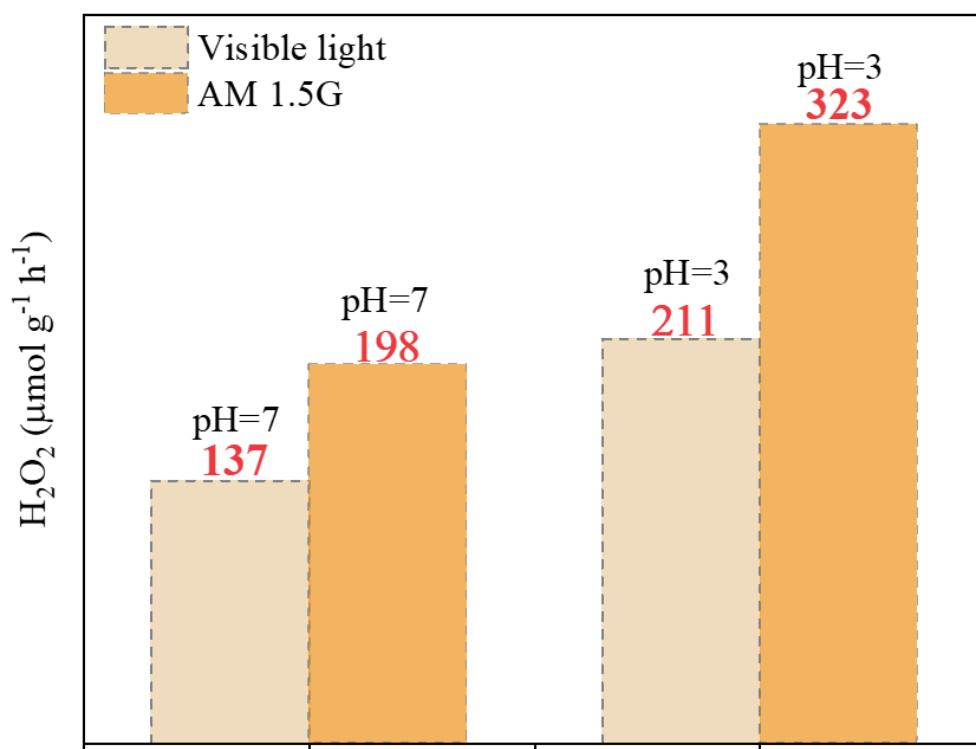
Fig. S20 Comparison of H_2O_2 generation rate of Nv-C≡N-CN under visible light ($\lambda \geq 420$ nm) and AM 1.5G.
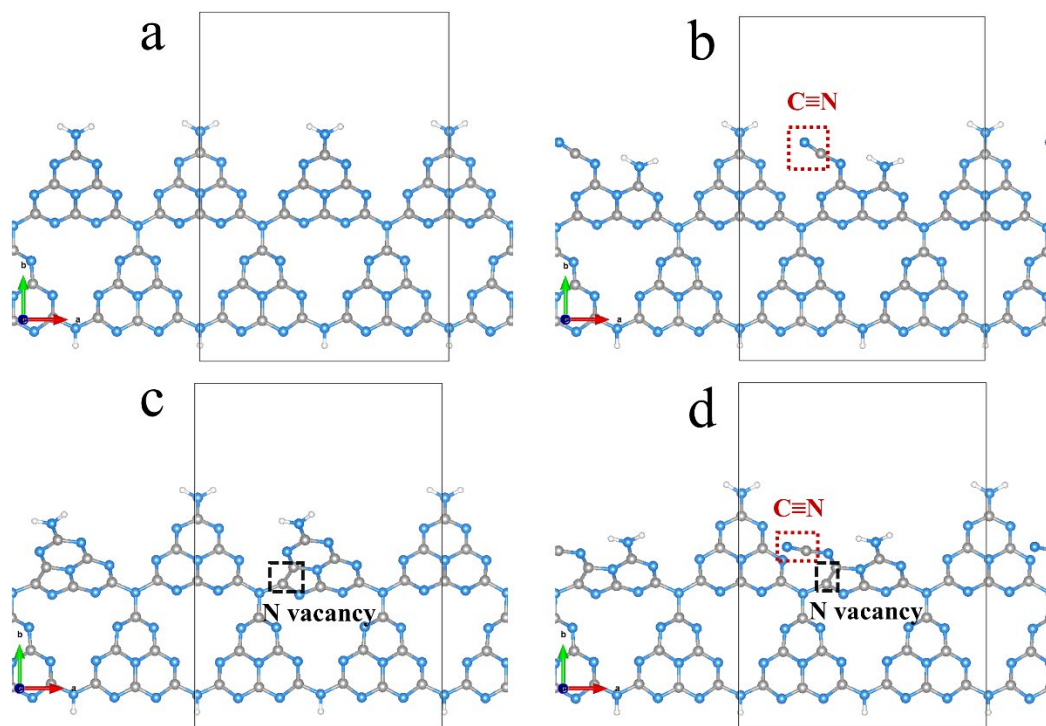
Fig. S21. The g-C$_3$N$_4$ models with different defect structures (The blue, gray, and white spheres are represented by N, C, and H atoms, respectively).

As shown in **Fig. S21**, **Fig. S21a-d** represents PCN, C≡N-CN, Nv-CN, and Nv-C≡N-CN, respectively.
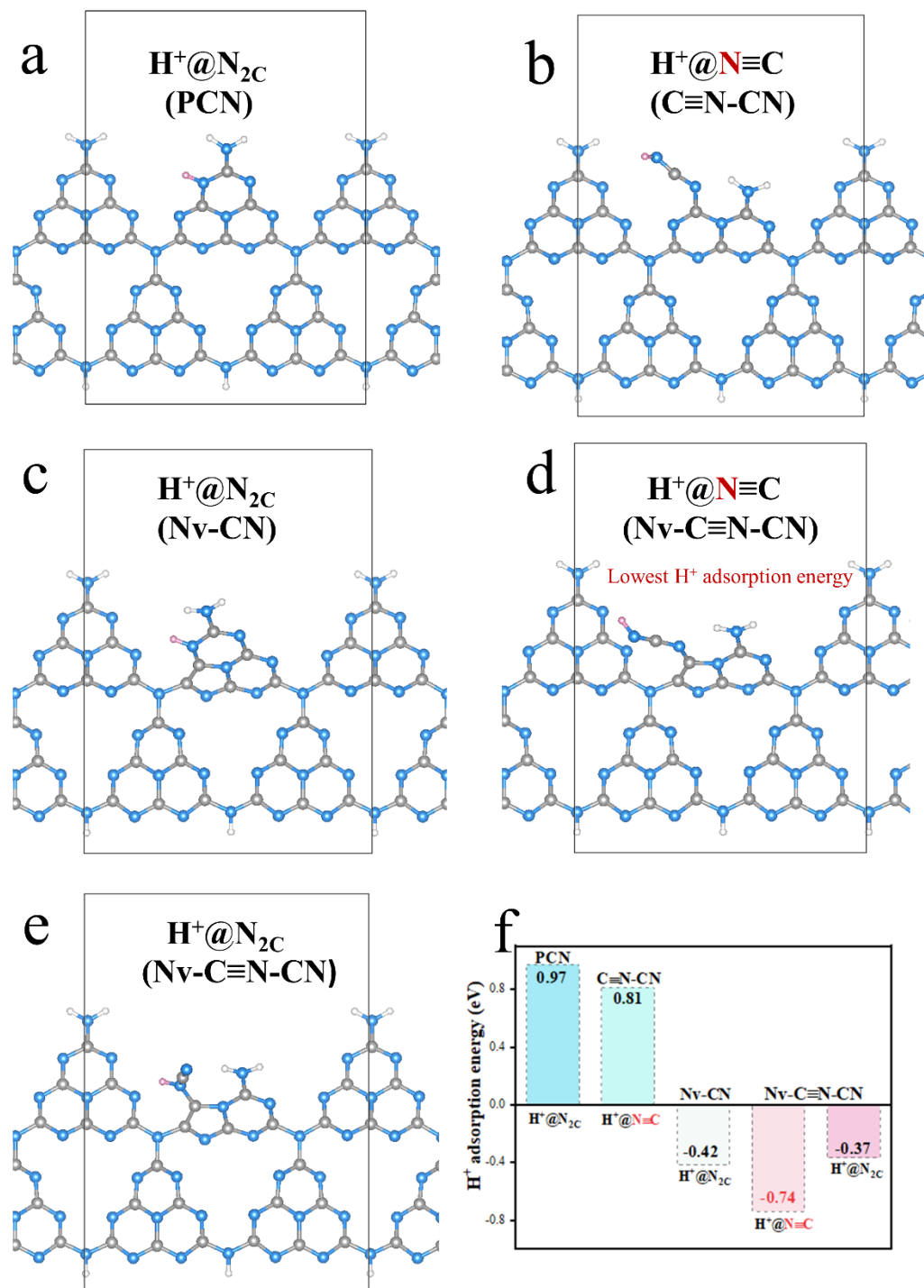
Fig. S22 The position of H$^+$ adsorption and the corresponding H$^+$ adsorption energy on g-C$_3$N$_4$ models with different defect structures. The pink spheres in **Fig. S22** represent the adsorbed H$^+$, which can be distinguished from the H atoms (white spheres) in g-C$_3$N$_4$ structure.

For ease of illustration, the corresponding H^+ adsorption energy was also organized in Figure S18f. As shown in **Fig. S22**, the H^+ adsorption sites are all on the N atoms of g-C_3N_4. Among them, H^+ is adsorbed on the N_{2C} atom in PCN, and then after the $-C\equiv N$ groups appears, H^+ is preferentially adsorbed on the N atom of $-C\equiv N$ in $C\equiv N$-CN; at the same time, the H^+ adsorption energy is reduced from 0.97 to 0.81 eV (**Fig. S22f**), indicating that the $-C\equiv N$ groups can effectively adsorb H^+ in this reaction. On Nv-$C\equiv N$-CN, H^+ is adsorbed on the N atoms of the $-C\equiv N$ groups and has the lowest H^+ adsorption energy of -0.74 eV. We additionally simulated the adsorption of H^+ on the N_{2C} position over Nv-$C\equiv N$-CN **(Fig. S22e)**, and its adsorption energy was -0.37 eV. This comparison clearly shows that H^+ is preferentially adsorbed at $-C\equiv N$ on Nv-$C\equiv N$-CN.
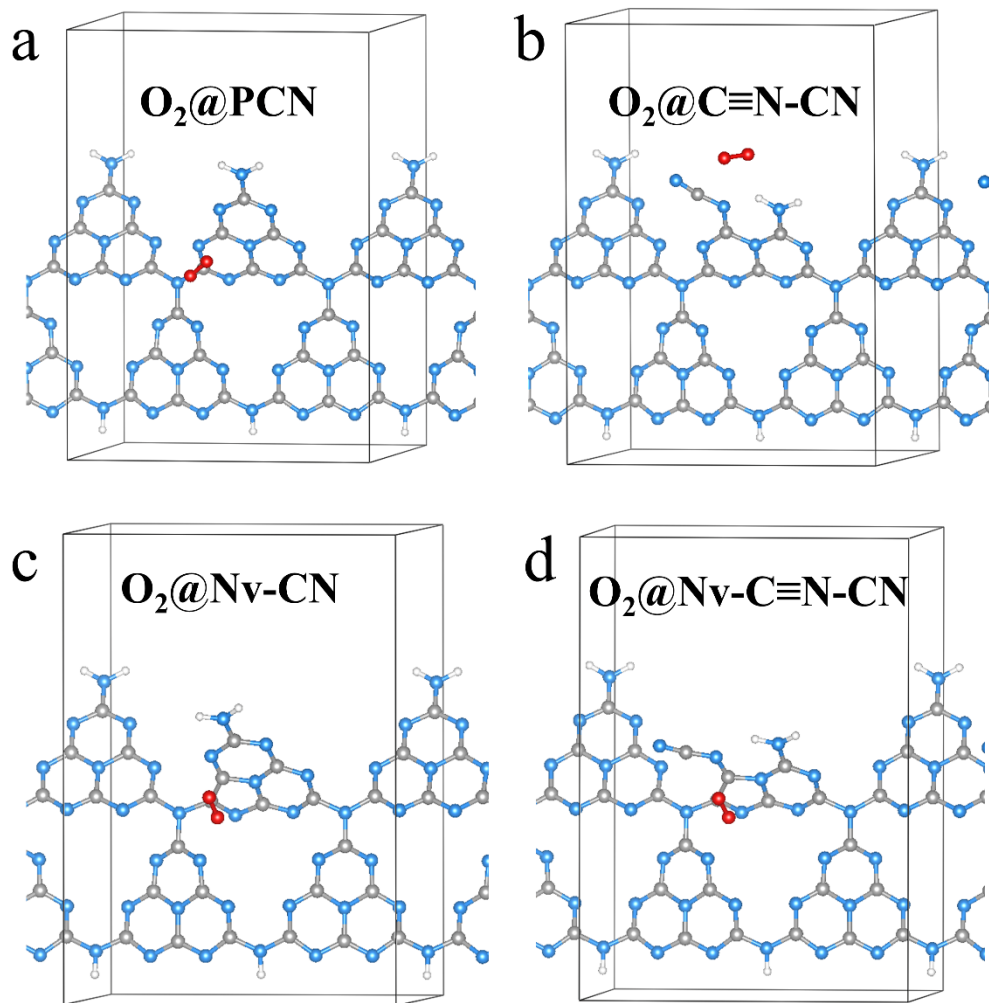
Fig. S23 The O_2 adsorption position on (a) PCN, (b) C≡N-CN, (c) Nv-CN, and (d) Nv-C≡N-CN.
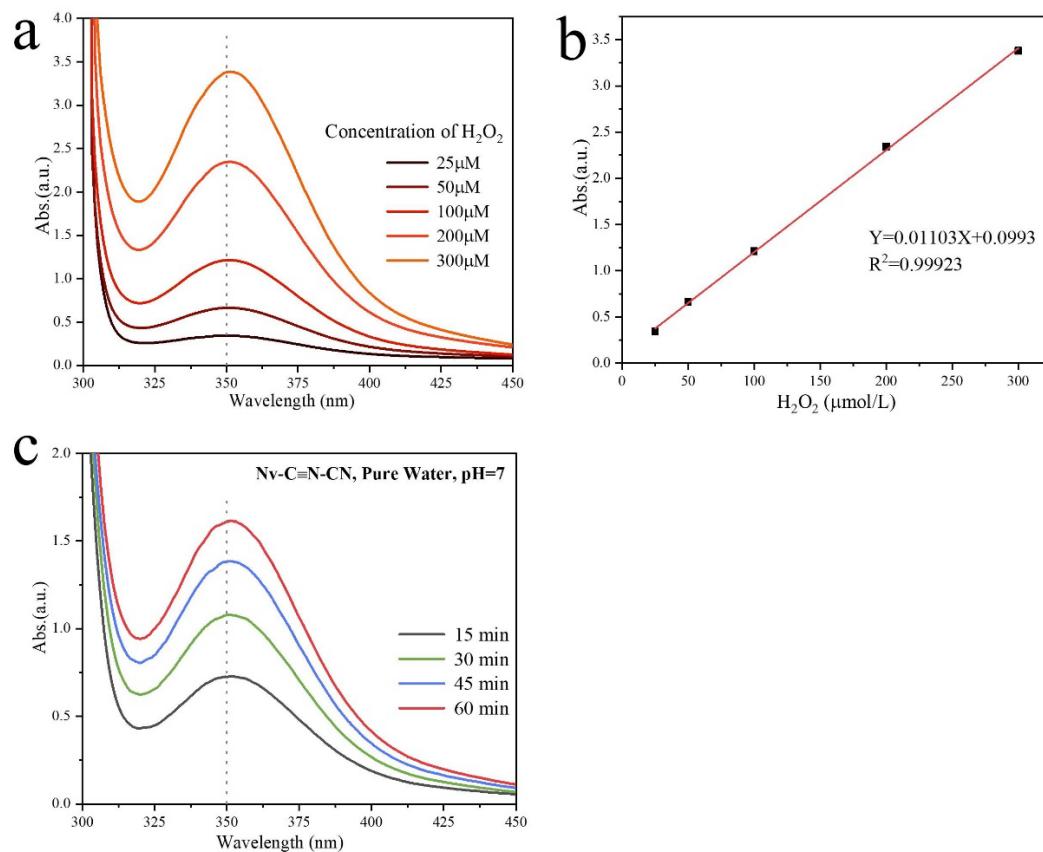
Fig. S24 (a) Determination of UV-vis absorption intensity of different H_2O_2 concentrations by iodimetry. (b) The linear fitting formula of standard H_2O_2 concentration. (c) The UV-vis spectrum changes of H_2O_2 generated by Nv-C≡N-CN in pure water under visible light ($\lambda \geq 420$ nm, pH=7).

3.2 Table S1-S9:

Table S1. XPS surface atoms ratio and N/C from OEA of C≡N-CN and Nv-C≡N-CN.

Samples	N/C	N₂c/C	N₃c/C	NHₓ/C	N₂c/N₃c	N/C (OEA)
C≡N-CN	**1.05**	**0.76**	0.23	0.06	**3.33**	1.76056
Nv-C≡N-CN	**0.73**	**0.37**	0.29	0.06	**1.27**	1.65645

Table S2. XPS data of all samples (the binding energy of different types of carbon and nitrogen in C1s and N1s).

Samples	N-C=N	C≡N/ C-NHₓ	C-C/C=C	NHₓ	N₃c	N₂c
PCN	288.5	286.4	284.8	401.5	400.3	398.9
TCN	288.4	286.4	284.8	401.5	400.4	398.9
C≡N-CN	288.5	286.5	284.8	401.5	400.3	398.9
Nv-C≡N-CN	288.5	286.4	284.8	401.5	400.1	398.9

Table S3. TRPL date of the samples.

Samples	τ_1/ns (A_1)	τ_2/ns (A_2)	τ_3/ns (A_3)	τ_A/ns[a]
PCN	1.25(27.99%)	4.87(50.72%)	28.10(21.29%)	8.80
TCN	0.83(26.22%)	3.94(47.63%)	19.92(26.15%)	7.31
C≡N-CN	0.85(29.16%)	4.17(49.12%)	21.97(21.72%)	7.07
Nv-C≡N-CN	0.59(24.68%)	3.51(47.40%)	17.27(27.93)	6.63

[a] The calculation formula of the average TRPL lifetime is: $\tau_A = \frac{\sum A_i \tau_i}{\sum A_i}$, where τ_i is the time coefficient and A_i is the corresponding amplitude of each component.

Table S4. BET specific surface areas ($m^2\ g^{-1}$) of the samples

Samples	PCN	TCN	C≡N-CN	Nv-C≡N-CN
BET ($m^2\ g^{-1}$)	55.0	11.4	46.9	150.5

Table S5. The wavelength-dependent AQY for photocatalytic H_2O_2 generation by Nv-C≡N-CN.[a]

Wavelength (nm)	400	420	450	500	550
H_2O_2 evolution (μmol)	2.241	1.645	0.745	0.588	0.210
Light intensity (mWcm^{-2})	12	14.5	10.2	12.6	14.8
Irradiation area (cm^2)	1.69	1.69	1.69	1.69	1.69
Irradiation time (h)	1	1	1	1	1
AQY (%)	3.1	1.8	1.1	0.6	0.2

[a] Conditions: $\lambda \geq 420$ nm; pure water, pH=7;1 g L^{-1} catalyst.

Table S6. SCC of the photocatalytic H_2O_2 generation by Nv-C≡N-CN under AM 1.5G simulated sunlight.[a]

H_2O_2 evolution (μmol)	Light intensity (mW/cm^2)	Irradiation area (cm^2)	Irradiation time (h)	SCC (%)
7.077	100	1	1	0.23

[a] Conditions: $\lambda \geq 420$ nm; pure water, pH=7;1 g L^{-1} catalyst.

SCC:

$$SCC = \frac{\left[\Delta G_{H_2O_2}\right] \times \left[n_{H_2O_2}\right]}{I \times S \times T} \times 100\% = \frac{117 \times 10^3 \times 7.077 \times 10^{-6}}{100 \times 1 \times 10^{-3} \times 3600} \times 100\%$$

$$= 0.23\%$$

Table S7. The wavelength-dependent AQY for photocatalytic H_2O_2 generation by Nv-C≡N-CN. Conditions: $\lambda \geq 420$ nm, 10% IPA, pH=3, 1 g L^{-1} catalyst.

Wavelength (nm)	400	420	450	500	550
H_2O_2 evolution (μmol)	26.137	20.245	8.768	6.539	1.347
Light intensity (mW cm^{-2})	12	14.5	10.2	12.6	14.8
Irradiation area (cm^2)	1.69	1.69	1.69	1.69	1.69
Irradiation time (h)	1	1	1	1	1
AQY (%)	36.2	22.1	12.7	6.9	1.1

λ=400 nm:

The number of incident photons: $N = \dfrac{E\lambda}{h\nu} = \dfrac{12\times10^{-3}\times3600\times400\times10^{-9}}{6.626\times10^{-34}\times3\times10^{8}} = 8.69303\times 10^{19}$

$AQY = \dfrac{2\times H_2O_2 \text{ formed (mol)}}{\text{the number of incident photons (mol)}} \times 100\ \% = \dfrac{2\times26.137\times10^{-6}\times6.02\times10^{23}}{8.69303\times10^{19}} \times 100\% = 36.2\%$

λ=420 nm:

The number of incident photons: $N = \dfrac{E\lambda}{h\nu} = \dfrac{14.5\times10^{-3}\times3600\times420\times10^{-9}}{6.626\times10^{-34}\times3\times10^{8}} = 1.10293\times 10^{20}$

$AQY = \dfrac{2\times H_2O_2 \text{ formed (mol)}}{\text{the number of incident photons (mol)}} \times 100\ \% = \dfrac{2\times20.245\times10^{-6}\times6.02\times10^{23}}{1.10293\times10^{20}} \times 100\% = 22.1\%$

Table S8. Summary of g-C$_3$N$_4$-based materials for photocatalytic H$_2$O$_2$ generation activity. The experimental system is subdivided into different pH, with or without sacrificial agent (EtOH is ethanol and IPA is isopropanol in this table), and different light intensity. The standardized yield of H$_2$O$_2$ (μmol/g/h), AQY, and SCC are used as evaluation indicators.

Catalysts	Sacrificial Reagent	Light Source	H$_2$O$_2$ yields (μmol/g/h)	AQY	SCC	Ref
Nv-C≡N-CN (This work)	**Pure water, pH=7**	**λ≥420 nm**	**137**	**3.1%(400nm) 1.8%(420nm)**	**0.23%**	
		AM 1.5G	**198**	**/**		
	Pure water, pH=3	**λ≥420 nm**	**211**	**/**		
		AM 1.5G	**323**			
	10% IPA, pH=3	**λ≥420 nm**	**3093**	**36.2%(400nm) 22.1%(420nm)**		
		AM 1.5G	**3930**	**/**		
CN$_4$	10% IPA	λ≥420 nm	574	13.9% (420 nm)		5
CO/AQ/C$_3$N$_4$	Pure water	AM 1.5G	124	0.051%	0.014%	6
PEI/g-C$_3$N$_4$	Pure water	AM 1.5G	208.1	2.1% (420nm)	0.045%	7
ZnPPC-NBCN	Pure water	λ≥420 nm	114	/	0.13%	8
Ag@U-g-C$_3$N$_4$	Pure water, pH=3	λ≥420 nm	70	/	/	9
CTF-BDDBN	Pure water	λ≥420 nm	97	/	/	10
CN/RGO@BPQDs	Pure water pH=6.5	λ≥420 nm	60.6	/	/	11
P-Mmcnns-25	5% EtOH	AM 1.5G	1083	0.045%(420nm)	/	12
AKMT	10% IPA	λ≥420 nm	2733	70% (420nm)	/	13
RF523	Pure water	λ≥420 nm	52	8%(420nm)	0.5%	14
OCN	Pure water	λ≥420 nm	105	/	/	1
	10% IPA	λ≥420 nm	1200	10.2%(420nm)	/	
DCN	20% IPA	λ≥420 nm	96.8	10.7%(420nm)	/	15
Ti$_2$C$_3$-g-C$_3$N$_4$	10% IPA	λ≥420 nm	131.71	/	/	16
K$_2$HPO$_4$/GCN	10% EtOH	λ≥420 nm	505	/	/	17
Mesoporous g-C$_3$N$_4$	90% EtOH	λ≥420 nm	183.5	/	/	18
3DM-g-C3N4-PW$_{11}$	Pure water	λ≥320 nm	35	/	/	19

g-C$_3$N$_4$/BDI	Pure water	λ≥420 nm	9.6	2.6%(420nm)	/	20
Cv-g-C$_3$N$_4$	Pure water	λ≥420 nm	92	/	/	21
G-CN-PWO	Pure water	λ≥420 nm	60	/	/	22
g-C$_3$N$_4$/PDI/rGO	Pure water	λ≥420 nm	24.1	/	0.2%	23
BP/CN	10% IPA	λ≥420 nm	540	/	/	24
SS-CN	10% IPA	λ≥420 nm	566.69	/	/	25
g-C$_3$N$_4$/PDI$_{151}$	Pure water	λ≥420 nm	21	/	/	26
KOH- g-C$_3$N$_4$	10% IPA	λ≥420 nm	704	/	/	27
IO-CN-Cv	5% EtOH	λ≥420 nm	162.87	/	/	28
Ultra-thin g-C$_3$N$_4$	10% EtOH	λ≥420 nm	43	0.54% (420nm)	/	29

Table S9. The O-O bond-length of adsorbed O$_2$ on various g-C$_3$N$_4$.[a]

O$_2$ adsorption position	PCN	C≡N-CN	Nv-CN	Nv-C≡N-CN
O-O bond-length	1.2432 Å	1.2397 Å	1.2563 Å	1.2546 Å

[a] The O-O bond-length of free O$_2$ is 1.2075 Å.

4. Reference

1. Z. Wei, M. Liu, Z. Zhang, W. Yao, H. Tan and Y. Zhu, *Energy & Environmental Science*, 2018, **11**, 2581-2589.
2. C. Fan, J. Miao, G. Xu, J. Liu, J. Lv and Y. Wu, *RSC Advances*, 2017, **7**, 37185-37193.
3. Y. Wang, P. Du, H. Pan, L. Fu, Y. Zhang, J. Chen, Y. Du, N. Tang and G. Liu, *Adv Mater*, 2019, **31**, e1807540.
4. H. Yu, R. Shi, Y. Zhao, T. Bian, Y. Zhao, C. Zhou, G. I. N. Waterhouse, L. Z. Wu, C. H. Tung and T. Zhang, *Adv Mater*, 2017, **29**.
5. C. Feng, L. Tang, Y. Deng, J. Wang, J. Luo, Y. Liu, X. Ouyang, H. Yang, J. Yu and J. Wang, *Advanced Functional Materials*, 2020, **30**.
6. C. Chu, Q. Zhu, Z. Pan, S. Gupta, D. Huang, Y. Du, S. Weon, Y. Wu, C. Muhich, E. Stavitski, K. Domen and J. H. Kim, *Proc Natl Acad Sci U S A*, 2020, **117**, 6376-6382.
7. X. Zeng, Y. Liu, Y. Kang, Q. Li, Y. Xia, Y. Zhu, H. Hou, M. H. Uddin, T. R. Gengenbach, D. Xia, C. Sun, D. T. McCarthy, A. Deletic, J. Yu and X. Zhang, *ACS Catalysis*, 2020, **10**, 3697-3706.
8. Y. X. Ye, J. Pan, F. Xie, L. Gong, S. Huang, Z. Ke, F. Zhu, J. Xu and G. Ouyang, *Proc Natl Acad Sci U S A*, 2021, **118**.

9. J. Cai, J. Huang, S. Wang, J. Iocozzia, Z. Sun, J. Sun, Y. Yang, Y. Lai and Z. Lin, *Adv Mater*, 2019, **31**, e1806314.

10. L. Chen, L. Wang, Y. Wan, Y. Zhang, Z. Qi, X. Wu and H. Xu, *Adv Mater*, 2020, **32**, e1904433.

11. J. Xiong, X. Li, J. Huang, X. Gao, Z. Chen, J. Liu, H. Li, B. Kang, W. Yao and Y. Zhu, *Applied Catalysis B: Environmental*, 2020, **266**.

12. L. Zhou, J. Feng, B. Qiu, Y. Zhou, J. Lei, M. Xing, L. Wang, Y. Zhou, Y. Liu and J. Zhang, *Applied Catalysis B: Environmental*, 2020, **267**.

13. P. Zhang, Y. Tong, Y. Liu, J. J. M. Vequizo, H. Sun, C. Yang, A. Yamakata, F. Fan, W. Lin, X. Wang and W. Choi, *Angew Chem Int Ed Engl*, 2020, **59**, 16209-16217.

14. Y. Shiraishi, T. Takii, T. Hagi, S. Mori, Y. Kofuji, Y. Kitagawa, S. Tanaka, S. Ichikawa and T. Hirai, *Nat Mater*, 2019, **18**, 985-993.

15. L. Shi, L. Yang, W. Zhou, Y. Liu, L. Yin, X. Hai, H. Song and J. Ye, *Small*, 2018, **14**.

16. Y. Yang, Z. Zeng, G. Zeng, D. Huang, R. Xiao, C. Zhang, C. Zhou, W. Xiong, W. Wang, M. Cheng, W. Xue, H. Guo, X. Tang and D. He, *Applied Catalysis B: Environmental*, 2019, **258**.

17. J. Tian, T. Wu, D. Wang, Y. Pei, M. Qiao and B. Zong, *Catalysis Today*, 2019, **330**, 171-178.

18. Y. Shiraishi, Y. Kofuji, H. Sakamoto, S. Tanaka, S. Ichikawa and T. Hirai, *ACS Catalysis*, 2015, **5**, 3058-3066.

19. S. Zhao, X. Zhao, H. Zhang, J. Li and Y. Zhu, *Nano Energy*, 2017, **35**, 405-414.

20. Y. Kofuji, S. Ohkita, Y. Shiraishi, H. Sakamoto, S. Tanaka, S. Ichikawa and T. Hirai, *ACS Catalysis*, 2016, **6**, 7021-7029.

21. S. Li, G. Dong, R. Hailili, L. Yang, Y. Li, F. Wang, Y. Zeng and C. Wang, *Applied Catalysis B: Environmental*, 2016, **190**, 26-35.

22. S. Zhao and X. Zhao, *Journal of Catalysis*, 2018, **366**, 98-106.

23. Y. Kofuji, Y. Isobe, Y. Shiraishi, H. Sakamoto, S. Tanaka, S. Ichikawa and T. Hirai, *J Am Chem Soc*, 2016, **138**, 10019-10025.

24. Y. Zheng, Z. Yu, H. Ou, A. M. Asiri, Y. Chen and X. Wang, *Advanced Functional Materials*, 2018, **28**.

25. C. Feng, L. Tang, Y. Deng, J. Wang, Y. Liu, X. Ouyang, H. Yang, J. Yu and J. Wang, *Applied Catalysis B: Environmental*, 2021, **281**.

26. Y. Shiraishi, S. Kanazawa, Y. Kofuji, H. Sakamoto, S. Ichikawa, S. Tanaka and T. Hirai, *Angew Chem Int Ed Engl*, 2014, **53**, 13454-13459.

27. H. Zhang, L. Jia, P. Wu, R. Xu, J. He and W. Jiang, *Applied Surface Science*, 2020, **527**.

28. J. Lei, B. Chen, W. Lv, L. Zhou, L. Wang, Y. Liu and J. Zhang, *ACS Sustainable Chemistry & Engineering*, 2019, **7**, 16467-16473.

29. W. Liu, C. Song, M. Kou, Y. Wang, Y. Deng, T. Shimada and L. Ye, *Chemical Engineering Journal*, 2021, **425**.